

# Noise Synthesis for Low-Light Image Denoising with Diffusion Models

Liying Lu    Raphaël Achddou    Sabine Süsstrunk  
 IVRL (Image and Visual Representation Lab), EPFL  
 {liying.lu, raphael.achddou, sabine.sustrunk}@epfl.ch

## Abstract

*Low-light photography produces images with low signal-to-noise ratios due to limited photons. In such conditions, common approximations like the Gaussian noise model fall short, and many denoising techniques fail to remove noise effectively. Although deep-learning methods perform well, they require large datasets of paired images that are impractical to acquire. As a remedy, synthesizing realistic low-light noise has gained significant attention. In this paper, we investigate the ability of diffusion models to capture the complex distribution of low-light noise. We show that a naive application of conventional diffusion models is inadequate for this task and propose three key adaptations that enable high-precision noise generation without calibration or post-processing: a two-branch architecture to better model signal-dependent and signal-independent noise, the incorporation of positional information to capture fixed-pattern noise, and a tailored diffusion noise schedule. Consequently, our model enables the generation of large datasets for training low-light denoising networks, leading to state-of-the-art performance. Through comprehensive analysis, including statistical evaluation and noise decomposition, we provide deeper insights into the characteristics of the generated data.*

## 1. Introduction

Obtaining noiseless photographs in low-light settings is extremely challenging. Although extending the exposure time can gather more light and enhance brightness in still scenes, this solution falls short for dynamic scenes due to the necessity of a static environment during image capture. Alternatively, increasing the system gain expands the RAW signal’s dynamic range, but this operation also dramatically increases the noise level in the captured image.

To address this, numerous deep-learning denoising methods [35, 46, 58] have been proposed. However, training deep networks requires substantial amounts of data, and acquiring paired noisy-clean image sets is both laborious and time-consuming. This process involves capturing a clean image with a long-exposure time and a noisy image with a short-exposure time under the same low-light condition. To



Figure 1. Denoising results from networks trained with synthetic data generated by different synthesis methods, with a network trained on paired real data included for reference. The sample image is from the ELD test set [52] (cropped for visualization). The effectiveness of trained denoiser strongly depends on the quality of the noise data used for training. Our approach is to utilize diffusion models to generate synthetic noise data that closely fits real situations in low-light scenarios, enabling the trained model to denoise images effectively. (Best viewed when zoomed in.)

ensure proper alignment, the camera must remain stationary and the scene must be free of moving objects. These strict conditions make data collection difficult and limit the dataset to static scenes.

As larger training datasets generally lead to better low-light denoising performance, the challenge of obtaining sufficient training data has become a prominent topic in the field. To address this bottleneck, a growing number of methods have embraced noise synthesis techniques that can be broadly categorized into physics-based and deep-learning based methods. In physics-based noise modeling, the prevalent Poisson-Gaussian noise model combines signal-dependent Poisson and signal-independent Gaussian distributions. Despite advances in physics-based noise modeling by subsequent works [12, 20, 48, 52, 57], a disparity persists between the synthesized and real noise distributions. Conversely, deep-learning-based noise modeling explores the application of generative neural networks for learning the intricate patterns of real-world noise, either using generative adversarial networks (GANs) [27, 37, 56] or normalizing flows [2]. However, GANs generally suffer from training

instability and struggle to learn multimodal distributions effectively [44]. Normalizing flows are limited in model architecture design and also face difficulties with highly multimodal distributions [6].

In contrast, diffusion models [14, 25, 42] have shown strong performance in capturing complex multi-modal data distributions. In this paper, we investigate their application to the task of low-light noise synthesis. While a direct application of conventional diffusion models proves inadequate for this task, our proposed framework achieves state-of-the-art noise synthesis performance thanks to several adaptations. We discuss the role of each adaptation by carefully analyzing various statistics of the generated noise in Sec. 4.4. Our contributions are as follows: (1) We demonstrate that a two-branch neural network is an effective approach for modeling signal-dependent and signal-independent noise. (2) We incorporate positional encoding to account for the spatially varying nature of signal-independent noise. (3) We show empirically and theoretically that the diffusion noise schedule is critical for accurately capturing the noise variance. (4) We obtain state-of-the-art low-light noise synthesis performance, leading to better denoising performance compared to models trained on data synthesized by other techniques, as illustrated in Fig. 1.

## 2. Related Work

**Image Denoising.** Image denoising remains a persistent challenge in computer vision and image processing. Traditional methods often rely on various image priors, such as sparsity [3, 16, 33, 34, 40, 53, 54, 60], self-similarity [8, 13], and smoothness [43]. Notably, BM3D [13] is still regarded as a standard approach due to its accuracy and robustness.

Recent advancements in deep learning have revolutionized the field of image denoising, with Convolutional Neural Networks (CNNs) surpassing traditional methods to set new benchmarks [22, 35, 46, 55, 58]. However, most of these works approximate the noise distribution as Gaussian, whereas real noise distributions are far more complex. More recent works [1, 4, 11, 19, 50] focus on using real-world datasets to train denoising models.

Although image denoising datasets are available [1, 4, 11], they have several limitations: (1) data quantity is limited due to the tedious process of acquiring real-world datasets of clean and noisy image pairs. (2) Samples often have similar content as they are captured in limited scenes. (3) They are restricted to still scenes, as clean and noisy images must be well-aligned. These limitations impede image-denoising models from attaining optimal performance, as effectively training deep neural networks requires extensive training data. Consequently, numerous studies have begun exploring realistic noise synthesis as an easier alternative to data acquisition for increasing data quantity.

**Physics-Based Noise Modeling.** The widely used Additive

White Gaussian Noise (AWGN) approximation can not model real-world noise correctly. A more realistic alternative is the Poisson-Gaussian noise model [5, 7, 20, 21], which better reflects the nature of noise in imaging sensors. This model decomposes noise into two components: a signal-dependent Poisson noise arising from the stochastic nature of photon capture, and a signal-independent Gaussian noise approximating sensor-readout and thermal noises.

This model remains unable to capture all relevant noise sources. Subsequent works [12, 20, 48, 52, 57] introduce more complex and accurate noise models. In addition to the previously mentioned noise sources, these models incorporate other components of real-world noise, such as fixed-pattern noise and color-biased read noise. Recently, the ELD paper [52] introduces a noise model that accounts for multiple noise sources. After calibration, this noise model was utilized to synthesize noisy data for training an image-denoising CNN. Despite these advancements in physical noise modeling, a discrepancy persists between synthetic and real-world noise. In particular, modeling the signal-independent component of real noise is extremely challenging.

To address this, Zhang *et al.* [59] propose to capture frames in a completely dark environment and sample pixel values from them to represent the signal-independent noise. Signal-dependent noise is modeled using a simple Poisson distribution. Similarly, Feng *et al.* [18] further propose a "dark shading" correction method utilizing these dark frames to reduce the complexity of real-world noise distribution. They capture hundreds of dark frames and compute the average as the *dark shading* at various ISOs, which represents a combination of black level error (BLE) [38] and fixed-pattern noise (FPN) [9, 26]. Subtracting this *dark shading* from noisy images eases the denoising process. Several subsequent works employ this approach to simplify noise modeling [10] or improve denoising performance [51]. However, dark frames are not always accessible. In this work, we assume such data is not available.

**Deep Learning-Based Noise Modeling.** Another research line focuses on using deep neural networks to capture real-world noise more precisely. C2N [27] proposes to train a generative adversarial network (GAN) [23] with unpaired noisy and clean images for noisy image generation. The Noise Flow method [2] introduces the use of normalizing flows [15, 28, 29] to model real-world RAW noise. [30] also adopts normalizing flows for noise modeling, but in the output sRGB space.

Recently, LRD [56] proposes modeling signal-dependent noise with a Poisson distribution and learning the signal-independent part with a GAN. The GAN loss enables synthesizing signal-independent noise without explicitly decomposing the full noise. Monakhova *et al.* [37] introduced a noise generator where statistical noise parameters of a physics-

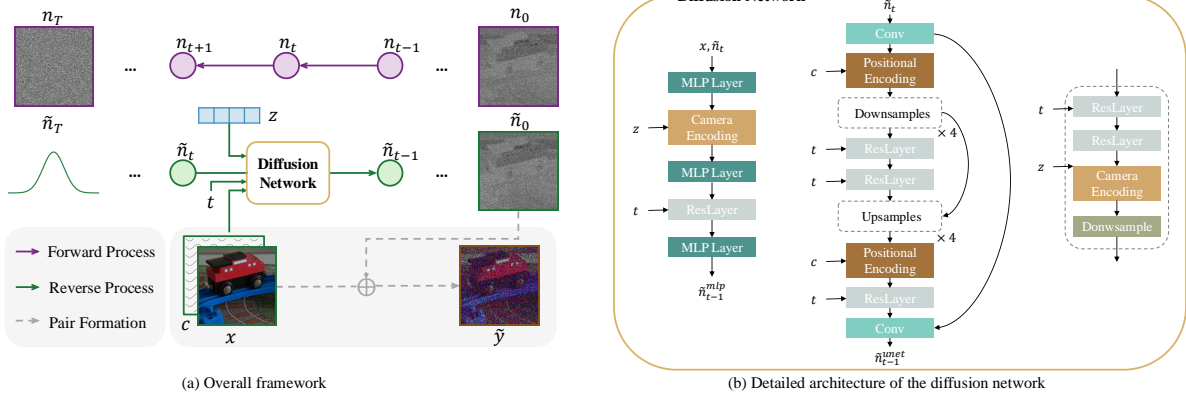


Figure 2. (a) The proposed diffusion framework for synthetic data generation. The forward process progressively destroys a real low-light noise  $\mathbf{n}_0$  by adding Gaussian noise. In the reverse process,  $\tilde{\mathbf{n}}_T$  is sampled from a Gaussian distribution and progressively denoised by a network back to the low-light noise  $\tilde{\mathbf{n}}_0$ . The network is conditioned on the clean image  $\mathbf{x}$ , pixel coordinates  $\mathbf{c}$ , and camera settings  $\mathbf{z}$ , as all these factors influence the noise pattern. Once the low-light noise  $\tilde{\mathbf{n}}_0$  is obtained, it can be added to the clean image  $\mathbf{x}$  to create the corresponding noisy image  $\tilde{\mathbf{y}}$ , thus forming a synthetic clean-noisy pair  $(\mathbf{x}, \tilde{\mathbf{y}})$ . (b) The detailed architecture of the two-branch diffusion network, shown from left to right: the MLP branch, the UNet branch, and the architecture of the down-sampling block (with up-sampling blocks having a similar structure).

based model are learned instead of manually calibrated.

Normalizing flows, however, struggle to capture highly multimodal or intricate structures in the data, and performance can be sensitive to the choice of flow architecture, hence necessitating careful tuning and experimentation [6]. As for GANs, they are notorious for their unstable training process [24, 36]. Diffusion models have demonstrated strong capabilities in modeling complex data distributions [39, 41, 42]. Therefore, in this paper, we investigate the use of diffusion models to model low-light noise to enable the generation of more realistic data samples.

### 3. Method

Conventional diffusion models for image generation cannot be naively adapted to low-light noise generation. We propose several key adaptations that enable high-precision noise generation. (Please refer to the appendix for preliminaries on diffusion models.)

#### 3.1. Framework for Low-light Noise Generation

Our model is trained on real noisy-clean RAW image pairs from the SID dataset [11]. The noisy image is captured with a short exposure time ( $\sim 0.1\text{s}$ ), while the clean image is captured with a long exposure time ( $\sim 10\text{s}$ ). In the following sections, we refer to the ratio between these exposure times as the *exposure ratio*.

The overall framework is depicted in Fig. 2 (a). The initial input for the forward process of the diffusion model is the low-light noise  $\mathbf{n}_0$ , obtained by subtracting the clean image from its noisy counterpart (which is obtained by multiplying the low-exposure image by the exposure ratio to match the

dynamic range of the clean image). Random samples of Gaussian noise are then added to  $\mathbf{n}_0$ , gradually approximating a standard normal distribution after  $T$  steps. For the backward process, a network is employed to predict the added Gaussian noise and denoise  $\tilde{\mathbf{n}}_T$  back to  $\tilde{\mathbf{n}}_0$ .

As signal-dependent noise is correlated to the clean image and camera settings, we condition our diffusion network on these factors. We also encode pixel positions into the diffusion network to better capture spatially related noise components, such as fixed-pattern noise, which is salient in low-light images. Hence, the reverse process of our diffusion model is formulated as  $\tilde{\mathbf{n}}_t = f_\theta(\tilde{\mathbf{n}}_{t-1}, t, \mathbf{x}, \mathbf{c}, \mathbf{z})$ , where  $t$  is the diffusion timestep,  $\mathbf{x}$  is the clean image,  $\mathbf{c}$  are the pixel coordinates, and  $\mathbf{z}$  is the camera setting (including ISO value and the exposure ratio). Conditioning the diffusion model on the clean image is done by concatenating it with the input noise image. Regarding the pixel coordinates, the camera settings, and the diffusion timestep, further explanation is provided in Sec. 3.2.

#### 3.2. Network Architecture

**Two-Branch Architecture.** We design our diffusion network with two branches as shown in Fig. 2 (b): a Multilayer perceptron (MLP) branch and a UNet branch. This design addresses the distinct nature of different noise components. Noise components such as shot noise only depend on the current clean pixel value. Hence, their generation should not be influenced by neighboring pixels, making the MLP branch well-suited for handling these characteristics. Conversely, noise components that are locally correlated are better captured by the UNet architecture that excels at modeling local

dependencies. In the experimental section, we will further validate the effectiveness of this design.

The MLP branch consists of three MLP layers, a camera setting encoding layer and a residual layer with diffusion timestep encoding. The UNet branch includes four down-sampling blocks and four up-sampling blocks. The UNet branch also includes a camera setting encoding layer, positional encoding layers, and diffusion timestep encoding layers. Next, we detail how these additional layers work.

**Positional Encoding.** As previously stated, signal-independent noise cannot be accurately represented by a Gaussian distribution alone. Low-light noise includes spatially correlated noise components, such as banding patterns and low-frequency noise [18, 52]. Fig. 6 presents two examples from the SID dataset. Banding patterns and a spatially varying offset at the bottom of the frame are visible, especially in the first example. We therefore integrate positional encoding in our diffusion network, so that the diffusion model becomes aware of pixel positions. We first use sinusoidal positional encoding [47] to encode the pixel coordinate map  $\mathbf{c}$ , and use  $1 \times 1$  convolutional layers to learn a scale and shift map  $\mathbf{s}$ ,  $\mathbf{r}$ , which are then integrated into the image feature as:  $\hat{\mathbf{f}} = \mathbf{f} \odot (1 + \mathbf{s}) + \mathbf{r}$ . We encode the diffusion timestep  $t$  in a similar fashion to that of positional encoding. For more details, please refer to the appendix.

**Camera Setting Encoding.** As camera settings (such as ISO value and exposure ratio) affect noise patterns, we encode this information into our network. We create a camera-setting embedding bank with a number (larger than the number of unique camera settings in the dataset) of randomly initialized embeddings, ensuring each setting has a distinct embedding. Each camera setting’s corresponding embedding  $\mathbf{z}$  is integrated with the image feature  $\mathbf{f}$  using cross-attention. More details are provided in the appendix.

As a result, these embeddings are optimized during training, effectively delivering the corresponding camera setting information to the network and ensuring it produces the appropriate noise pattern. This approach eliminates the need to train separate networks for each camera setting.

### 3.3. Variance Preserving Noise Schedule

Accurately modeling the noise variance is crucial for low-light noise generation as the slightest shift would impair the results of our subsequent denoising task. In this section, we explore the effects of various diffusion noise schedules and show the importance of selecting an appropriate schedule for generating low-light noise with precise variance.

Diffusion models use a predefined noise schedule to control the amount of Gaussian noise added to the input data (for details, please refer to the appendix). We observed that the commonly used cosine noise schedule [42] reduces the variance of the generated noise.

**MMSE Denoising Leads to Reduced Variance.** During

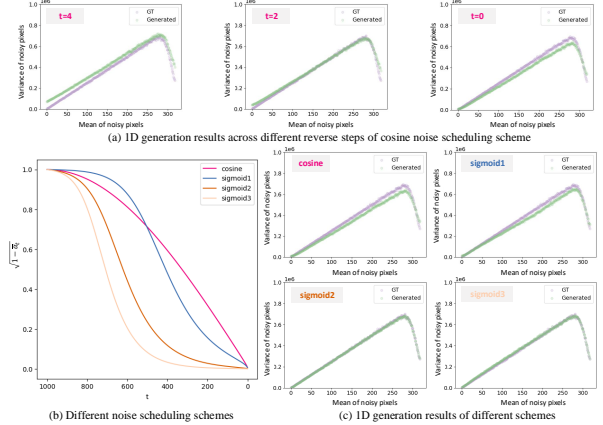


Figure 3. Impact of noise schedules. (a) Visualization of the mean-variance correspondences of the **real** and **generated** Poisson noises across different reverse steps ( $t = 4, 2, 0$ ) under the cosine noise-scheduling scheme. (b) Different noise scheduling schemes, the y-axis denotes the coefficient  $\sqrt{1 - \alpha_t}$  of the noise part in Eq. 3 of the appendix. (c) Results of different noise scheduling schemes, where *sigmoid2* and *sigmoid3* perform the best in our 1D toy example. Zoom in for a clearer view.

the reverse diffusion process, the diffusion network is trained to denoise the result from the previous timestep using the mean-squared-error (MSE) loss. However, it is known that the output of a denoising network trained with MSE loss is the expectation of all potential clean solutions [17, 31, 32]. Additionally, higher noise levels make the problem more ill-posed, thus resulting in a smoother denoised outcome.

Formally, consider the denoising problem where a measurement  $v$  is related to the signal  $u \sim U$  by  $v = u + \epsilon$ , with  $\epsilon \sim \mathcal{N}(0, \sigma_1^2)$  representing the Gaussian noise (added during the forward diffusion process). In our context, the target distribution  $U$  we aim to recover is the low-light noise distribution. For simplicity, here we assume that  $U$  follows a normal distribution  $\mathcal{N}(\lambda, \sigma_2^2)$ . The goal is to learn a denoiser  $f$  (i.e., the diffusion network) to recover  $u$  from  $v$ , given knowledge of  $\sigma_1$ .

**Proposition 1** (Proof in the appendix.). *When the denoiser is trained using the MSE loss, the optimal solution is given by  $f_{MMSE}(v) = \mathbb{E}[u|v]$ , and the variance of the solution is equal to  $\frac{\sigma_2^4}{\sigma_2^2 + \sigma_1^2}$ .*

As  $\sigma_1^2$  increases, the variance of the synthesized noise decreases. Therefore, to preserve the variance of  $U$ ,  $\sigma_1^2$  should be minimized. In other words, in the final steps of the reverse process (where the diffusion model focuses more on high-frequency details [49]), the diffusion model should be exposed to minimal Gaussian noise; otherwise, the generated output will be overly smoothed. Next, we validate this hypothesis through experiments on a 1D toy example by testing different noise schedules.

Dataset	Ratio	<i>Real-noise-based</i>	Physics-based		DNN-based		
		<i>Paired data</i>	Poisson-Gaussian	ELD [52]	NoiseFlow [2]	LRD [56]	Ours
Results without any post-processing							
SID	×100	42.40 / 0.958	39.79 / 0.929	<u>41.21 / 0.952</u>	38.42 / 0.917	39.93 / 0.924	<b>42.55 / 0.957</b>
	×250	39.68 / 0.942	34.71 / 0.863	<u>38.54 / 0.929</u>	34.22 / 0.850	35.42 / 0.857	<b>39.67 / 0.943</b>
	×300	36.95 / 0.927	31.74 / 0.783	<u>35.35 / 0.908</u>	32.07 / 0.784	32.50 / 0.783	<b>37.24 / 0.927</b>
ELD	×100	44.75 / 0.975	42.73 / 0.908	<u>45.06 / 0.975</u>	42.61 / 0.937	44.09 / 0.938	<b>45.13 / 0.973</b>
	×200	41.04 / 0.895	39.00 / 0.831	<b>43.20 / 0.954</b>	39.35 / 0.871	40.99 / 0.879	<u>41.36 / 0.912</u>
Results post-processed by the illumination correction method used in the ELD paper							
SID	×100	42.95 / 0.958	41.05 / 0.936	<u>41.95 / 0.953</u>	40.21 / 0.925	40.97 / 0.930	<b>43.30 / 0.958</b>
	×250	40.27 / 0.943	36.63 / 0.885	<u>39.44 / 0.931</u>	36.15 / 0.870	37.00 / 0.875	<b>40.53 / 0.944</b>
	×300	37.32 / 0.928	33.34 / 0.811	<u>36.36 / 0.911</u>	33.27 / 0.803	33.74 / 0.803	<b>37.68 / 0.928</b>
ELD	×100	45.52 / 0.977	44.02 / 0.931	<u>45.45 / 0.975</u>	43.31 / 0.941	44.56 / 0.946	<b>45.79 / 0.972</b>
	×200	41.70 / 0.912	41.00 / 0.880	<b>43.43 / 0.954</b>	40.26 / 0.885	41.71 / 0.899	<u>42.25 / 0.924</u>

Table 1. Quantitative evaluation of the SID and ELD datasets in terms of PSNR and SSIM across various exposure ratios. Results are provided for two cases: one without any post-processing, and another post-processed using the illumination correction method from the ELD paper. Best results are highlighted in **bold**, and second-best results are underlined. Our method outperforms all other synthesis methods across most settings.

**Performance of Different Noise Schedules.** For simplicity, we use a 1D Poisson distribution as a basic approximation of real-world noise. We train a 1D diffusion model using a 1D UNet to approach this distribution. The diffusion model employs the commonly used cosine noise schedule, which is plotted in Fig. 3 (b) in pink.

In Fig. 3 (a), we present the results of ground-truth and generated Poisson noises at different reverse steps (the last 4th, 2nd and final steps are shown for clarity). As the variance and mean values of a Poisson distribution are linearly related, we visualize this correspondence. Note that the visible tails are due to the clipping operation, where pixels saturate. We observe that the distribution of the generated results approaches the ground truth as the reverse steps progress ( $t \rightarrow 0$ ). However, after the final reverse step, one can observe that the variance of the generated Poisson noise consistently remains lower than that of the true Poisson distribution. Based on the explanation provided by Proposition 1, this observation can be attributed to the cosine noise schedule, which introduces excessive Gaussian noise at the beginning of the forward process. Consequently, at the end of the reverse process, the diffusion network must contend with an excessive amount of noise, leading to overly smooth outputs.

As noise schedule is crucial for accurately mapping the noise variance, we investigate various schedules with smoother slopes at the end of the backward process (with small  $t$ ). As depicted in Fig. 3 (b) and (c), we experiment with four different schemes. We observe that the smoother the slope of the curve at the end of the backward process, the better the results are in terms of variance preservation. Based on these observations, we empirically set the noise schedule to *sigmoid2* for subsequent experiments (*sigmoid3*

can also be chosen as it has similar performance).

## 4. Experimental Results

### 4.1. Evaluation Protocols

**Image Denoising Performance.** A direct approach to assess the quality of the noisy images generated by our model is to train a denoising network with them. We can then evaluate its performance on standard low-light denoising test sets. We compute the Peak Signal-to-Noise Ratio (PSNR) and Structural SIMilarity (SSIM) between the denoised and ground-truth images in the RAW domain.

**Noise Statistics.** We also analyze the pixel-wise marginal distributions between the generated and real noise images in the test set, similar to the approach presented in the Noise Flow paper [2]. This evaluation prioritizes the model’s ability to capture the fundamental characteristics of the noise distribution. Specifically, we compute the histograms of real-world and generated noise and report the discrete KL divergence between these histograms.

We further analyze the characteristics of the generated noise by evaluating its variance and mean values. For each possible clean pixel value, we gather the corresponding noise pixels and compute their mean and variance. The specific process is given in the appendix.

### 4.2. Implementation Details

We generate noise images in a patch-wise manner. Since our diffusion network is trained on  $512 \times 512$  patches, the generated noise patches are also  $512 \times 512$ . We use DDPM sampling [25] for inference.

We train our diffusion model using the SID Sony RAW

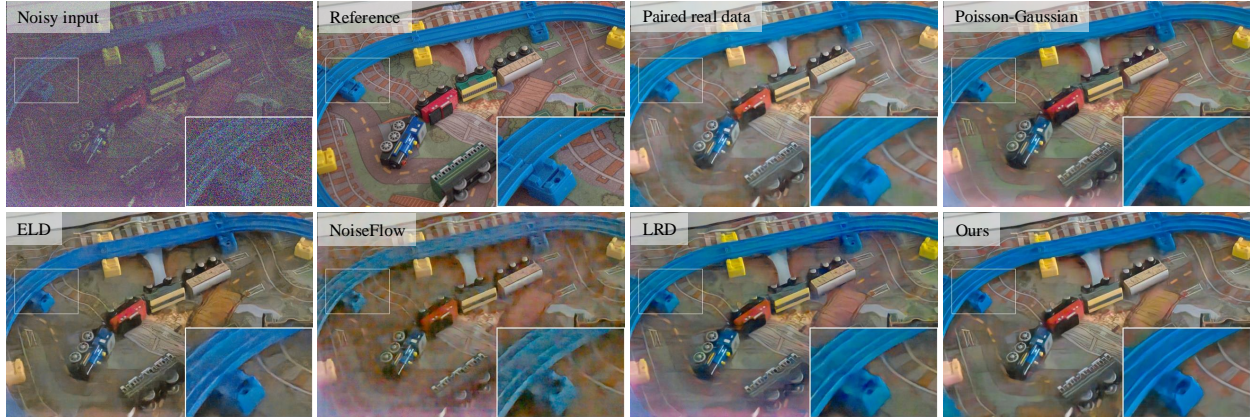


Figure 4. Visual comparison of denoising results from networks trained on data synthesized using different methods, alongside comparisons with a model trained on real clean-noisy pairs from the SID training set. The test sample is from the SID test set. All results here are processed by the same gamma correction for visualization purposes. Our method produces clearer details and effectively addresses the low-frequency noise at the bottom of the image, whereas other methods produce purplish artifacts. (Best viewed when zoomed in)

image training set. For evaluation, in line with the approach used in the ELD paper [52], we evaluate our denoising network on a combination of the SID test and validation sets (referred to as the SID test set hereafter), using the same evaluation images as in the ELD paper. We also evaluate our model on the ELD Sony dataset. Further implementation details are provided in the appendix.

### 4.3. Image Denoising Performance Comparison

As stated in Sec. 4.1, we compare the performance of denoising networks trained with data from different synthesis methods. We test two physics-based methods (the Poisson-Gaussian model and ELD [52]), and two recent learning-based methods (LRD [56] and NoiseFlow [2])<sup>1</sup>. Notably, our evaluation differs from ELD and LRD in two key ways:

- ELD crops the image centers to a size of  $512 \times 512$  for PSNR/SSIM computation, whereas we compute them on the entire image at a resolution of  $4240 \times 2832$ .
- In LRD’s image denoising code, a precomputed dark shading frame, which is computed by averaging multiple dark frames as mentioned in Sec. 2, is subtracted from the noisy images before denoising<sup>2</sup>. We omit this step, as such data is unavailable in usual cases.

In the following results, we apply the same measurement setup for all methods.

**Numerical Results.** Table 1 presents quantitative comparisons between different methods. The upper part of the table shows results obtained without any post-processing, where the denoised images are directly evaluated using classic metrics. The lower part presents the results after post-processing.

<sup>1</sup>For ELD and LRD, we use pre-trained models available on the authors’ official websites. For NoiseFlow, we retrain it on the SID dataset.

<sup>2</sup>See this part of the [code](#).

Since PSNR and SSIM metrics are sensitive to overall image illumination, even minor shifts can lead to significant variations in these values. We apply the illumination correction method from the ELD paper [52]<sup>3</sup> to the denoised images of all methods before evaluating their PSNR and SSIM.

Our approach achieves the best results on the SID dataset compared to other data synthesis techniques. It also outperforms the model trained with real data pairs in most cases. On the ELD test set, our method shows the best performance at the  $\times 100$  exposure ratio among all data synthesis approaches. However, our method achieves relatively lower PSNR/SSIM results than ELD at the  $\times 200$  exposure ratio (though still outperforming the learning-based LRD method and comparable to the real paired data). This is because the ELD method generates noisy images by sampling noise parameters from a realistic distribution, thus covering a broader range of noise levels. As our diffusion model was not trained with data from the  $\times 200$  exposure ratio (as this ratio is not present in the SID dataset), its generalization capability is somewhat limited. However, as we will show in the qualitative analysis, our method still produces denoised images with less noise and better detail preservation compared to other methods. The primary discrepancy is a color shift, which is a potential area for future improvement.

**Qualitative Results.** We compare denoising networks on an example from the SID test set in Fig. 4. While other noise synthesis methods struggle with low-frequency noise that appears at the bottom of the image, our method addresses this effectively. Visual comparisons on the ELD test set in Fig. 1 show that our method recovers the text details more clearly than other methods. Additional examples are given in the appendix.

<sup>3</sup>See this part of the [code](#).

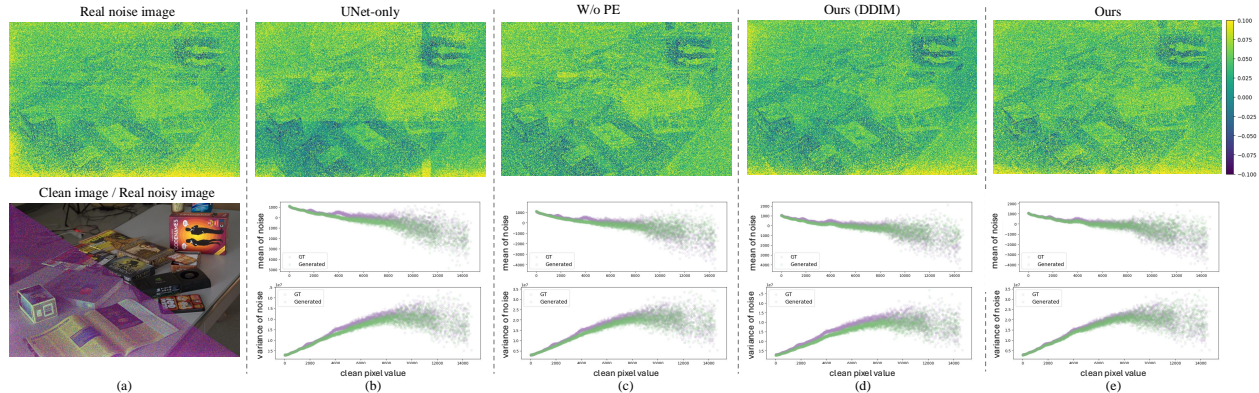


Figure 5. Ablation study on network architectures and diffusion sampling methods. (a) Second row: a real clean-noisy pair from the SID Sony test set (ISO 10,000, ratio 250); first row: the corresponding real noise image. (b) Results from the UNet-only architecture. First row: generated noise image (by piecing  $512 \times 512$  patches together); second row: comparison of the mean and variance of the **generated noise** and the **real noise**. (c) Results from the network without positional encoding. (d) Results from the full network using DDIM sampling. (e) Results from our full network using DDPM sampling. The UNet-only architecture produces noise with inaccurate mean and variance. Without positional encoding, the network fails to model the low-frequency noise at the image bottom. DDIM sampling leads to reduced noise variance. Our full model generates the most accurate noise pattern.

Ratio	Ours (Limited data)	Ours
$\times 100$	42.42 / 0.956	42.55 / 0.957
$\times 250$	39.80 / 0.941	39.67 / 0.943
$\times 300$	36.87 / 0.924	37.24 / 0.927

Table 2. Ablation study on the influence of training-data diversity for denoising. We show the PSNR/SSIM results on the SID test set.

#### 4.4. Discussions

In this section, we assess the importance of various components in our diffusion model by analyzing the characteristics of the generated noise and the denoising performance of networks trained on data generated by ablated models

**Influence of Training-Data Diversity.** The number of scenes per camera setting in the SID training set is uneven, with some settings having more than ten scenes and some only one (e.g., 28 scenes for ISO 250 and 1 for ISO 2500). To evaluate the influence of training-data diversity, we train a denoising network on synthetic data using the same number of scenes per camera setting as in the SID training set. The results, reported as *Ours (Limited data)* in Table 2, are unsurprisingly close to those obtained when training on paired real data, as shown in Table 1.

To leverage the full potential of our diffusion model, we generate more synthetic data by randomly sampling scenes from the SID dataset, regardless of their camera settings. This sampling strategy improves image denoising performance, as shown in Table 2. Visual comparisons in the appendix further support that it improves the results for under-represented camera settings. Thus, our method offers a promising approach for improving denoising performance when real-world data is scarce.

**Sampling Method.** The generation speed of our method

	(A)	(B)	(C)	(D)
Exposure Ratio	<i>UNet-only (DDIM)</i>	<i>W/o PE (DDIM)</i>	<i>Full network (DDIM)</i>	<i>Full network (DDPM)</i>
$\times 100$	41.45 / 0.953 <i>0.645</i>	41.64 / 0.948 <i>0.622</i>	42.03 / 0.953 <i>0.622</i>	<b>42.42 / 0.956</b> <b>0.568</b>
$\times 250$	39.22 / 0.936 <i>0.016</i>	38.94 / 0.925 <i>0.011</i>	39.44 / 0.937 <i>0.008</i>	<b>39.80 / 0.941</b> <b>0.004</b>
$\times 300$	36.59 / 0.915 <i>0.028</i>	35.99 / 0.898 <i>0.022</i>	36.67 / 0.916 <i>0.019</i>	<b>36.87 / 0.924</b> <b>0.018</b>

Table 3. Ablation study on network architectures and diffusion sampling methods. We present the PSNR/SSIM results of denoising networks trained with different synthetic data sources generated by various methods on the SID test set. We also report the KL divergence (in *italic*) between the noise distributions produced by these methods and the real noise distribution.

is constrained by the many steps required by DDPM sampling. Therefore, in the following ablation studies, we use DDIM sampling [45] as an alternative, which uses a non-Markovian framework to achieve faster generation with fewer steps. We first validate that DDIM could achieve satisfactory performance with a minor drop compared to DDPM. We train a denoising network with synthetic data generated using 100-step DDIM sampling. As shown in Fig. 5 (d), DDIM generates noise resembling real noise, with slight variance inaccuracy. Table 3 (C) and (D) show that while DDIM introduces a performance trade-off, the decrease is acceptable.

**Effects of Two-Branch Network Architecture.** We investigate the effects of our proposed two-branch network architecture by conducting an ablation study, which adopts a sole UNet architecture for the diffusion model. This UNet-only architecture takes the clean image  $\mathbf{x}$  and the output of

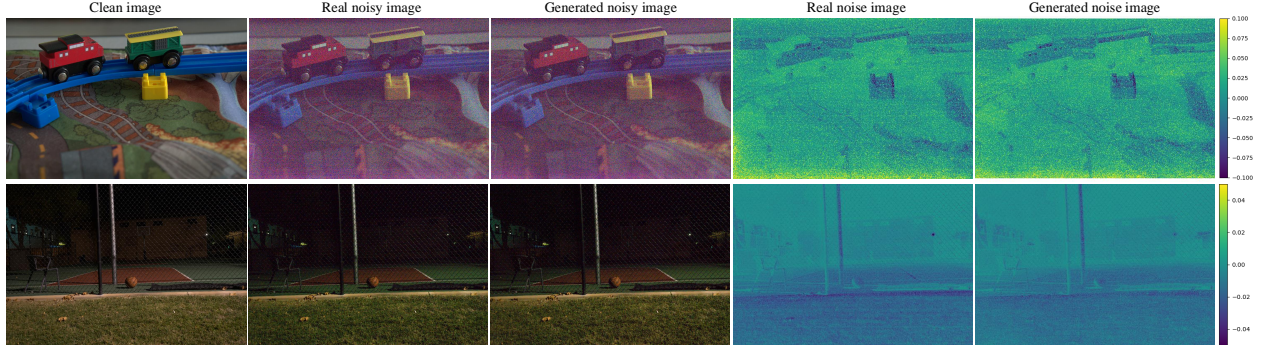


Figure 6. Comparison between real and synthetic data. The samples in the two rows are from the SID Sony test set (not used for diffusion training) under the following settings: ISO 6,400 with a ratio of 300; and ISO 200 with a ratio of 250. Different noise values are represented by varying colors, with the color bar displayed on the right. Our method generates realistic noise that closely resembles real noise.

the last step  $\tilde{\mathbf{n}}_t$  as inputs; it then outputs the result of the current step  $\tilde{\mathbf{n}}_{t-1}$ . To assess performance differences, we generate synthetic data from clean images in the SID training set using both architectures with DDIM sampling for efficiency. We then compare the performance of two denoising networks trained on these respective synthetic datasets, as shown in Table 3. Comparing (A) and (C) shows that the full network achieves higher PSNR/SSIM. Additionally, the full model’s noise has a smaller KL divergence from real noise than the UNet-only model. We also condition both architectures on the same clean images from the SID test set and visualize the generated results. Examples are shown in Fig. 5 (b) and (e). Note that our diffusion network generates patches of  $512 \times 512$  size. To visualize the full image, we piece patches together. The noise patches produced by the UNet-only architecture exhibit a checkerboard pattern; this indicates inconsistent mean values among patches. This phenomenon suggests that the UNet-only architecture generates noise images with unstable mean values.

**Effects of Positional Encoding.** We further investigate the effects of positional encoding. We conduct the following experiment to assess its effects: During inference, we modify the generation process to  $\tilde{\mathbf{n}}_t = f_\theta(\tilde{\mathbf{n}}_{t-1}, t, \mathbf{x}, \mathbf{0}, \mathbf{z})$ , where  $\mathbf{0}$  denotes a black image filled with zeros, signifying that the diffusion model is conditioned on a zero map instead of on the exact pixel coordinates. We compare KL divergence of noise generated by models with and without positional encoding. Table 3 (B) and (C) show that the denoising network trained with data generated with positional encoding yields higher PSNR and SSIM, and the KL divergence increases when positional encoding is not used. The generated results are depicted in Fig. 5 (c). By comparing it with the full results in Fig. 5 (e), it can be observed that the generated noises do not contain the low-frequency noise in the bottom; this indicates the effectiveness of positional encoding in modeling the position-related noises.

**Noise Visualization.** In Fig. 6, we visualize noise images

generated by our model. By comparing real and generated noise, we demonstrate that our diffusion model accurately captures realistic noise patterns. In the first sample, the real noise image exhibits low-frequency noise at the bottom. Our model successfully reproduces this, as the generated noise also shows low-frequency noise at the bottom. Failure to capture this pattern would result in a purplish offset in the final denoised images. As shown in Fig. 4, our denoising network effectively handles low-frequency noise, unlike other methods, which produce purplish artifacts at the bottom.

**Noise Decomposition.** Our framework enables noise decomposition, allowing for further analysis of generated-noise characteristics by separating it into signal-dependent and signal-independent components. Our findings suggest that this method can implicitly produce dark frames, and it points toward a potential approach for efficient data generation in future work. See the appendix for details.

## 5. Conclusion and Limitations

Diffusion models have been widely applied for generating realistic images, but their use for generating real-world noise remains unexplored. Nonetheless, We find that a direct application of diffusion models is insufficient for realistic noise synthesis. Our tailored diffusion framework enables generating synthetic noise that closely matches real-world noise, thus outperforming existing noise synthesis methods. Moreover, our analysis of the generated data provides valuable insights into using diffusion models for real-world noise synthesis. Despite the promising results, our method also shows some limitations in generalization, especially in generalizing to unseen camera settings. Future work could improve generalization by integrating physics-based noise modeling with our diffusion-based approach. Generation speed is also a constraint; while DDIM sampling offers some acceleration, it still incorrectly maps the noise variance. Consequently, faster and more accurate approaches could be explored.

## References

- [1] Abdelrahman Abdelhamed, Stephen Lin, and Michael S Brown. A high-quality denoising dataset for smartphone cameras. In *Proceedings of the IEEE Conference on Computer Vision and Pattern Recognition*, pages 1692–1700, 2018. [ii](#)
- [2] Abdelrahman Abdelhamed, Marcus A Brubaker, and Michael S Brown. Noise flow: Noise modeling with conditional normalizing flows. In *Proceedings of the IEEE/CVF International Conference on Computer Vision*, pages 3165–3173, 2019. [i](#), [ii](#), [v](#), [vi](#)
- [3] Michal Aharon, Michael Elad, and Alfred Bruckstein. K-svd: An algorithm for designing overcomplete dictionaries for sparse representation. *IEEE Transactions on Signal Processing*, 54(11):4311–4322, 2006. [ii](#)
- [4] Josue Anaya and Adrian Barbu. Renoir—a dataset for real low-light image noise reduction. *Journal of Visual Communication and Image Representation*, 51:144–154, 2018. [ii](#)
- [5] Nicolas Bähler, Majed El Helou, Étienne Objois, Kaan Okumuş, and Sabine Süsstrunk. Pogain: Poisson-gaussian image noise modeling from paired samples. *IEEE Signal Processing Letters*, 29:2602–2606, 2022. [ii](#)
- [6] Sam Bond-Taylor, Adam Leach, Yang Long, and Chris G Willcocks. Deep generative modelling: A comparative review of vaes, gans, normalizing flows, energy-based and autoregressive models. *IEEE Transactions on Pattern Analysis and Machine Intelligence*, 44(11):7327–7347, 2021. [ii](#), [iii](#)
- [7] Tim Brooks, Ben Mildenhall, Tianfan Xue, Jiawen Chen, Dillon Sharlet, and Jonathan T Barron. Unprocessing images for learned raw denoising. In *Proceedings of the IEEE/CVF Conference on Computer Vision and Pattern Recognition*, pages 11036–11045, 2019. [ii](#)
- [8] Antoni Buades, Bartomeu Coll, and J-M Morel. A non-local algorithm for image denoising. In *2005 IEEE Computer Society Conference on Computer Vision and Pattern Recognition (CVPR’05)*, pages 60–65. Ieee, 2005. [ii](#)
- [9] Stephen C Cain, Majeed M Hayat, and Ernest E Armstrong. Projection-based image registration in the presence of fixed-pattern noise. *IEEE Transactions on Image Processing*, 10(12):1860–1872, 2001. [ii](#)
- [10] Yue Cao, Ming Liu, Shuai Liu, Xiaotao Wang, Lei Lei, and Wangmeng Zuo. Physics-guided iso-dependent sensor noise modeling for extreme low-light photography. In *Proceedings of the IEEE/CVF Conference on Computer Vision and Pattern Recognition*, pages 5744–5753, 2023. [ii](#)
- [11] Chen Chen, Qifeng Chen, Jia Xu, and Vladlen Koltun. Learning to see in the dark. In *Proceedings of the IEEE Conference on Computer Vision and Pattern Recognition*, pages 3291–3300, 2018. [ii](#), [iii](#), [xiii](#), [xiv](#), [xv](#)
- [12] Roberto Costantini and Sabine Süsstrunk. Virtual sensor design. In *Sensors and Camera Systems for Scientific, Industrial, and Digital Photography Applications V*, pages 408–419. SPIE, 2004. [i](#), [ii](#)
- [13] Kostadin Dabov, Alessandro Foi, Vladimir Katkovnik, and Karen Egiazarian. Image denoising by sparse 3-d transform-domain collaborative filtering. *IEEE Transactions on Image Processing*, 16(8):2080–2095, 2007. [ii](#)
- [14] Prafulla Dhariwal and Alexander Nichol. Diffusion models beat gans on image synthesis. *Advances in Neural Information Processing Systems*, 34:8780–8794, 2021. [ii](#)
- [15] Laurent Dinh, Jascha Sohl-Dickstein, and Samy Bengio. Density estimation using real nvp. *arXiv preprint arXiv:1605.08803*, 2016. [ii](#)
- [16] Michael Elad and Michal Aharon. Image denoising via sparse and redundant representations over learned dictionaries. *IEEE Transactions on Image Processing*, 15(12):3736–3745, 2006. [ii](#)
- [17] Michael Elad, Bahjat Kawar, and Gregory Vaksman. Image denoising: The deep learning revolution and beyond—a survey paper. *SIAM Journal on Imaging Sciences*, 16(3):1594–1654, 2023. [iv](#)
- [18] Hansen Feng, Lizhi Wang, Yuzhi Wang, and Hua Huang. Learnability enhancement for low-light raw denoising: Where paired real data meets noise modeling. In *Proceedings of the 30th ACM International Conference on Multimedia*, pages 1436–1444, 2022. [ii](#), [iv](#), [xvi](#)
- [19] Roman Flepp, Andrey Ignatov, Radu Timofte, and Luc Van Gool. Real-world mobile image denoising dataset with efficient baselines. In *Proceedings of the IEEE/CVF Conference on Computer Vision and Pattern Recognition*, pages 22368–22377, 2024. [ii](#)
- [20] Alessandro Foi. Clipped noisy images: Heteroskedastic modeling and practical denoising. *Signal Processing*, 89(12):2609–2629, 2009. [i](#), [ii](#)
- [21] Alessandro Foi, Mejdi Trimeche, Vladimir Katkovnik, and Karen Egiazarian. Practical poissonian-gaussian noise modeling and fitting for single-image raw-data. *IEEE Transactions on Image Processing*, 17(10):1737–1754, 2008. [ii](#)
- [22] Michaël Gharbi, Gaurav Chaurasia, Sylvain Paris, and Frédo Durand. Deep joint demosaicking and denoising. *ACM Transactions on Graphics (ToG)*, 35(6):1–12, 2016. [ii](#)
- [23] Ian Goodfellow, Jean Pouget-Abadie, Mehdi Mirza, Bing Xu, David Warde-Farley, Sherjil Ozair, Aaron Courville, and Yoshua Bengio. Generative adversarial nets. *Advances in Neural Information Processing Systems*, 27, 2014. [ii](#)
- [24] Ishaan Gulrajani, Faruk Ahmed, Martin Arjovsky, Vincent Dumoulin, and Aaron C Courville. Improved training of wasserstein gans. *Advances in Neural Information Processing Systems*, 30, 2017. [iii](#)
- [25] Jonathan Ho, Ajay Jain, and Pieter Abbeel. Denoising diffusion probabilistic models. *Advances in Neural Information Processing Systems*, 33:6840–6851, 2020. [ii](#), [v](#), [xii](#), [xv](#)
- [26] Gerald C Holst. Cmos/ccd sensors and camera systems. *CMOS/CCD Sensors and Camera Systems/Gerald C. Holst*, 2007. [ii](#)
- [27] Geonwoon Jang, Wooseok Lee, Sanghyun Son, and Kyoung Mu Lee. C2n: Practical generative noise modeling for real-world denoising. In *Proceedings of the IEEE/CVF International Conference on Computer Vision*, pages 2350–2359, 2021. [i](#), [ii](#)
- [28] Durk P Kingma and Prafulla Dhariwal. Glow: Generative flow with invertible 1x1 convolutions. *Advances in Neural Information Processing Systems*, 31, 2018. [ii](#)

- [29] Ivan Kobyzev, Simon JD Prince, and Marcus A Brubaker. Normalizing flows: An introduction and review of current methods. *IEEE Transactions on Pattern Analysis and Machine Intelligence*, 43(11):3964–3979, 2020. [ii](#)
- [30] Shayan Kousha, Ali Maleky, Michael S Brown, and Marcus A Brubaker. Modeling srgb camera noise with normalizing flows. In *Proceedings of the IEEE/CVF Conference on Computer Vision and Pattern Recognition*, pages 17463–17471, 2022. [ii](#)
- [31] Christian Ledig, Lucas Theis, Ferenc Huszár, Jose Caballero, Andrew Cunningham, Alejandro Acosta, Andrew Aitken, Alykhan Tejani, Johannes Totz, Zehan Wang, et al. Photo-realistic single image super-resolution using a generative adversarial network. In *Proceedings of the IEEE Conference on Computer Vision and Pattern Recognition*, pages 4681–4690, 2017. [iv](#)
- [32] J Lehtinen. Noise2noise: Learning image restoration without clean data. *arXiv preprint arXiv:1803.04189*, 2018. [iv](#)
- [33] Julien Mairal, Michael Elad, and Guillermo Sapiro. Sparse representation for color image restoration. *IEEE Transactions on Image Processing*, 17(1):53–69, 2007. [ii](#)
- [34] Julien Mairal, Francis Bach, Jean Ponce, Guillermo Sapiro, and Andrew Zisserman. Non-local sparse models for image restoration. In *2009 IEEE 12th International Conference on Computer Vision*, pages 2272–2279. IEEE, 2009. [ii](#)
- [35] Xiaojiao Mao, Chunhua Shen, and Yu-Bin Yang. Image restoration using very deep convolutional encoder-decoder networks with symmetric skip connections. *Advances in Neural Information Processing Systems*, 29, 2016. [i](#), [ii](#)
- [36] Lars Mescheder, Andreas Geiger, and Sebastian Nowozin. Which training methods for gans do actually converge? In *International Conference on Machine Learning*, pages 3481–3490. PMLR, 2018. [iii](#)
- [37] Kristina Monakhova, Stephan R Richter, Laura Waller, and Vladlen Koltun. Dancing under the stars: video denoising in starlight. In *Proceedings of the IEEE/CVF Conference on Computer Vision and Pattern Recognition*, pages 16241–16251, 2022. [i](#), [ii](#)
- [38] Junichi Nakamura. *Image sensors and signal processing for digital still cameras*. CRC press, 2017. [ii](#)
- [39] Ben Poole, Ajay Jain, Jonathan T Barron, and Ben Mildenhall. Dreamfusion: Text-to-3d using 2d diffusion. *arXiv preprint arXiv:2209.14988*, 2022. [iii](#)
- [40] Javier Portilla, Vasily Strela, Martin J Wainwright, and Eero P Simoncelli. Image denoising using scale mixtures of gaussians in the wavelet domain. *IEEE Transactions on Image Processing*, 12(11):1338–1351, 2003. [ii](#)
- [41] Aditya Ramesh, Prafulla Dhariwal, Alex Nichol, Casey Chu, and Mark Chen. Hierarchical text-conditional image generation with clip latents. *arXiv preprint arXiv:2204.06125*, 1(2): 3, 2022. [iii](#)
- [42] Robin Rombach, Andreas Blattmann, Dominik Lorenz, Patrick Esser, and Björn Ommer. High-resolution image synthesis with latent diffusion models. In *Proceedings of the IEEE/CVF Conference on Computer Vision and Pattern Recognition*, pages 10684–10695, 2022. [ii](#), [iii](#), [iv](#)
- [43] Leonid I Rudin, Stanley Osher, and Emad Fatemi. Nonlinear total variation based noise removal algorithms. *Physica D: Nonlinear Phenomena*, 60(1-4):259–268, 1992. [ii](#)
- [44] Antoine Salmona, Valentin De Bortoli, Julie Delon, and Agnes Desolneux. Can push-forward generative models fit multimodal distributions? *Advances in Neural Information Processing Systems*, 35:10766–10779, 2022. [ii](#)
- [45] Jiaming Song, Chenlin Meng, and Stefano Ermon. Denoising diffusion implicit models. *arXiv preprint arXiv:2010.02502*, 2020. [vii](#), [xv](#)
- [46] Ying Tai, Jian Yang, Xiaoming Liu, and Chunyan Xu. Memnet: A persistent memory network for image restoration. In *Proceedings of the IEEE International Conference on Computer Vision*, pages 4539–4547, 2017. [i](#), [ii](#)
- [47] A Vaswani. Attention is all you need. *Advances in Neural Information Processing Systems*, 2017. [iv](#), [xiii](#)
- [48] Hans B Wach and Edward R Dowski. Noise modeling for design and simulation of color imaging systems. In *Color and Imaging Conference*, pages 211–216. Society of Imaging Science and Technology, 2004. [i](#), [ii](#)
- [49] Binxu Wang and John J Vastola. Diffusion models generate images like painters: an analytical theory of outline first, details later. *arXiv preprint arXiv:2303.02490*, 2023. [iv](#)
- [50] Yuzhi Wang, Haibin Huang, Qin Xu, Jiaming Liu, Yiqun Liu, and Jue Wang. Practical deep raw image denoising on mobile devices. In *European Conference on Computer Vision*, pages 1–16. Springer, 2020. [ii](#)
- [51] Yufei Wang, Yi Yu, Wenhao Yang, Lanqing Guo, Lap-Pui Chau, Alex C Kot, and Bihan Wen. Exposediffusion: Learning to expose for low-light image enhancement. In *Proceedings of the IEEE/CVF International Conference on Computer Vision*, pages 12438–12448, 2023. [ii](#)
- [52] Kaixuan Wei, Ying Fu, Yinqiang Zheng, and Jiaolong Yang. Physics-based noise modeling for extreme low-light photography. *IEEE Transactions on Pattern Analysis and Machine Intelligence*, 44(11):8520–8537, 2021. [i](#), [ii](#), [iv](#), [v](#), [vi](#), [xiii](#)
- [53] Qi Xie, Qian Zhao, Deyu Meng, and Zongben Xu. Kronecker-basis-representation based tensor sparsity and its applications to tensor recovery. *IEEE Transactions on Pattern Analysis and Machine Intelligence*, 40(8):1888–1902, 2017. [ii](#)
- [54] Jun Xu, Lei Zhang, and David Zhang. A trilateral weighted sparse coding scheme for real-world image denoising. In *Proceedings of the European Conference on Computer Vision (ECCV)*, pages 20–36, 2018. [ii](#)
- [55] Syed Waqas Zamir, Aditya Arora, Salman Khan, Munawar Hayat, Fahad Shahbaz Khan, and Ming-Hsuan Yang. Restormer: Efficient transformer for high-resolution image restoration. In *Proceedings of the IEEE/CVF Conference on Computer Vision and Pattern Recognition*, pages 5728–5739, 2022. [ii](#)
- [56] Feng Zhang, Bin Xu, Zhiqiang Li, Xinran Liu, Qingbo Lu, Changxin Gao, and Nong Sang. Towards general low-light raw noise synthesis and modeling. In *Proceedings of the IEEE/CVF International Conference on Computer Vision*, pages 10820–10830, 2023. [i](#), [ii](#), [v](#), [vi](#)
- [57] Jiachao Zhang and Keigo Hirakawa. Improved denoising via poisson mixture modeling of image sensor noise. *IEEE Transactions on Image Processing*, 26(4):1565–1578, 2017. [i](#), [ii](#)
- [58] Kai Zhang, Wangmeng Zuo, Yunjin Chen, Deyu Meng, and Lei Zhang. Beyond a gaussian denoiser: Residual learning of

- deep cnn for image denoising. *IEEE Transactions on Image Processing*, 26(7):3142–3155, 2017. [i](#), [ii](#)
- [59] Yi Zhang, Hongwei Qin, Xiaogang Wang, and Hongsheng Li. Rethinking noise synthesis and modeling in raw denoising. In *Proceedings of the IEEE/CVF International Conference on Computer Vision*, pages 4593–4601, 2021. [ii](#)
- [60] Mingyuan Zhou, Haojun Chen, Lu Ren, Guillermo Sapiro, Lawrence Carin, and John Paisley. Non-parametric bayesian dictionary learning for sparse image representations. *Advances in Neural Information Processing Systems*, 22, 2009. [ii](#)

## Appendix

This appendix is organized as follows:

- Preliminaries: Diffusion Models → Sec. A
- Proof for Variance Preserving Noise Schedule → Sec. B
- Implementation Details → Sec. C
  - Network Architecture → Sec. C.1
  - Datasets → Sec. C.2
  - Training Configurations → Sec. C.3
  - Clean-Noisy Pair Generation → Sec. C.4
- Evaluation Protocol: Noise Mean and Variance → Sec. D
- More Discussions → Sec. E
  - Influence of Training-Data Diversity → Sec. E.1
  - Sampling Method → Sec. E.2
  - Noise Decomposition → Sec. E.3
  - Noise Histogram → Sec. E.4
- More Visual Comparisons → Sec. F

For optimal visual comparisons, we recommend viewing the results on a screen. We will release our code upon acceptance.

### A. Preliminaries: Diffusion Models

In this section, we review diffusion models [25]. Diffusion models involve a forward process and a reverse process. The *forward process*, also called *diffusion process*, formulates the posterior distribution  $q(x_{1:T}|x_0)$  as a Markov chain that gradually adds Gaussian noises to the input data  $x_0$ , according to a noise schedule  $\beta_1, \dots, \beta_T$ :

$$q(\mathbf{x}_{1:T}|\mathbf{x}_0) = \prod_{t=1}^T q(\mathbf{x}_t|\mathbf{x}_{t-1}), \quad (1)$$

$$q(\mathbf{x}_t|\mathbf{x}_{t-1}) = \mathcal{N}(\mathbf{x}_t; \sqrt{1 - \beta_t}\mathbf{x}_{t-1}, \beta_t\mathbf{I}), \quad (2)$$

where  $\mathbf{x}_t$  is the noised data at timestep  $t$ , and  $\mathcal{N}$  denotes the Gaussian distribution. An important property of the forward process is that we can sample  $\mathbf{x}_t$  at an arbitrary timestep  $t$ , directly from  $\mathbf{x}_0$  by

$$\mathbf{x}_t = \sqrt{\bar{\alpha}_t}\mathbf{x}_0 + \sqrt{(1 - \bar{\alpha}_t)}\epsilon_t, \quad (3)$$

where  $\epsilon_t \sim \mathcal{N}(0, \mathbf{I})$ ,  $\alpha_t = 1 - \beta_t$ , and  $\bar{\alpha}_t = \prod_{s=1}^t \alpha_s$ .

The *reverse process* estimates the joint distribution  $p_\theta(\mathbf{x}_{0:T})$ , starting from  $\mathbf{x}_T \sim \mathcal{N}(0, \mathbf{I})$ , it can be formulated as follows:

$$p_\theta(\mathbf{x}_{0:T}) = p_\theta(\mathbf{x}_T) \prod_{t=1}^T p_\theta(\mathbf{x}_{t-1}|\mathbf{x}_t), \quad (4)$$

$$\text{where } p_\theta(\mathbf{x}_{t-1}|\mathbf{x}_t) = \mathcal{N}(\mathbf{x}_{t-1}; \mu_\theta(\mathbf{x}_t, t), \Sigma_\theta\mathbf{I}), \quad (5)$$

where  $\Sigma_\theta = \frac{1 - \bar{\alpha}_{t-1}}{1 - \bar{\alpha}_t}\beta_t$ , and according to Ho *et al.* [25],  $\mu_\theta(\mathbf{x}_t, t)$  can be obtained by estimating the noise  $\epsilon_t$  added to  $\mathbf{x}_t$ , through a neural network  $\theta$ :

$$\mu_\theta(\mathbf{x}_t, t) = \frac{1}{\sqrt{\alpha_t}}(\mathbf{x}_t - \frac{\beta_t}{\sqrt{1 - \bar{\alpha}_t}}\epsilon_\theta(\mathbf{x}_t, t)). \quad (6)$$

The network parameters  $\theta$  are optimized by minimizing the following MSE loss:

$$\mathcal{L} = \mathbb{E}_q [\|\epsilon_t - \epsilon_\theta(\mathbf{x}_t, t)\|_2^2].$$

### B. Proof for Variance Preserving Noise Schedule

In this section, we present the proof of Proposition 1 discussed in the main paper.

*Proof.* Given a signal  $u \sim \mathcal{N}(\lambda, \sigma_2^2)$  and its measurement  $v = u + \epsilon$ , where  $\epsilon \sim \mathcal{N}(0, \sigma_1^2)$ , the conditional distribution of  $p(U|V)$  is

$$p(U|V = v) \sim \mathcal{N}\left(\lambda + \frac{\sigma_2^2}{\sigma_2^2 + \sigma_1^2}(v - \lambda), \frac{\sigma_2^2\sigma_1^2}{\sigma_2^2 + \sigma_1^2}\right). \quad (7)$$

In the reverse process, the goal of the diffusion model is to find the estimator  $\hat{u} = f(v)$  that minimizes the MSE

$$\text{MSE} = \mathbb{E} [\|u - \hat{u}\|_2^2 | v] = \int \|u - f(v)\|_2^2 p(u|v) du. \quad (8)$$

Taking the derivative of this expression with respect to  $f(v)$  and setting it to zero

$$\frac{d}{df(v)} \int \|u - f(v)\|_2^2 p(u|v) du \quad (9)$$

$$= -2 \int (u - f(v)) p(u|v) du = 0. \quad (10)$$

This simplifies to

$$\int u p(u|v) du = f(v) \int p(u|v) du = f(v). \quad (11)$$

Thus, the closed-form solution for the minimum mean squared error (MMSE) estimator is

$$f_{\text{MMSE}}(v) = \mathbb{E}[u|v] . \quad (12)$$

From Eq. 7, the explicit form of the MMSE estimator is

$$f_{\text{MMSE}}(v) = \lambda + \frac{\sigma_2^2}{\sigma_2^2 + \sigma_1^2} (v - \lambda) . \quad (13)$$

The variance of the MMSE solution is

$$\begin{aligned} \text{Var} \left( \lambda + \frac{\sigma_2^2}{\sigma_2^2 + \sigma_1^2} (V - \lambda) \right) &= \left( \frac{\sigma_2^2}{\sigma_2^2 + \sigma_1^2} \right)^2 \text{Var}(V) \\ &= \left( \frac{\sigma_2^2}{\sigma_2^2 + \sigma_1^2} \right)^2 (\text{Var}(U) + \sigma_1^2) \\ &= \frac{\sigma_2^4}{\sigma_2^2 + \sigma_1^2} . \end{aligned} \quad (14)$$

□

As previously discussed, in our context, the target distribution  $U$  that we aim to recover in the reverse process is the low-light noise distribution. For simplicity, we approximate it as a Gaussian distribution without sacrificing generality. Since the primary components of low-light noise (such as shot noise, read noise, and banding patterns) are either inherently modeled as Poisson distributions or can be approximated by Gaussian distributions [52]. Moreover, with a sufficient photon count, a Poisson distribution can be approximated by a Gaussian, as a consequence of the central limit theorem.

## C. Implementation Details

This section provides additional information about the detailed network architecture, the datasets used for training and evaluation, the training configurations for our diffusion model and denoising network, and the process for generating synthetic pairs.

### C.1. Network Architecture

In this section, we show the details of the positional encoding and camera setting encoding for integrating pixel coordinate and camera setting information into the diffusion model.

**Positional Encoding.** To integrate pixel coordinate information into our diffusion network, we propose to use positional encoding. We first use sinusoidal positional encoding [47] to encode the pixel coordinates as

$$\tilde{\mathbf{c}} = \text{Conv}_{1 \times 1}(\mathbf{c}) , \quad (15)$$

$$\mathbf{p} = \text{Conv}_{1 \times 1}([\tilde{\mathbf{c}}, \sin(\tilde{\mathbf{c}}), \cos(\tilde{\mathbf{c}})]) , \quad (16)$$

where  $\mathbf{c}$  is the coordinate map of the image pixels,  $\mathbf{p}$  is the resulting positional embedding,  $\text{Conv}_{1 \times 1}()$  denotes a convolutional layer with kernel size  $1 \times 1$ , and  $[ ]$  denotes the concatenation in the channel dimension.

Subsequently, the positional embedding is integrated into the image feature  $\mathbf{f}$  as

$$\mathbf{s}, \mathbf{r} = \text{Chunk}(\text{Conv}_{1 \times 1}(\mathbf{p})) , \quad (17)$$

$$\tilde{\mathbf{f}} = \mathbf{f} \odot (1 + \mathbf{s}) + \mathbf{r} , \quad (18)$$

where  $\odot$  is the element-wise multiplication, and  $\text{Chunk}()$  represents the operation that splits the feature map into two chunks in the channel dimension with the same channel number. The learned features  $\mathbf{s}$  and  $\mathbf{r}$  are used to scale and shift the image feature.

**Camera Setting Encoding.** Each camera setting’s corresponding embedding  $\mathbf{z}$  is integrated with the image feature  $\mathbf{f}$  using cross-attention as

$$\mathbf{Q} = \mathbf{f}\mathbf{W}_Q, \mathbf{K} = \mathbf{z}\mathbf{W}_K, \mathbf{V} = \mathbf{z}\mathbf{W}_V , \quad (19)$$

$$\tilde{\mathbf{f}} = \mathbf{f} + \text{Softmax}\left(\frac{\mathbf{Q}\mathbf{K}^T}{\sqrt{d}}\right)\mathbf{V} , \quad (20)$$

where  $\mathbf{W}_Q$ ,  $\mathbf{W}_K$  and  $\mathbf{W}_V$  are convolution layers with  $1 \times 1$  kernels, and  $d$  is the channel dimension of the  $\mathbf{Q}$  and  $\mathbf{K}$ .

### C.2. Datasets

We use the SID Sony dataset to train and evaluate our network. It comprises indoor and outdoor scenes captured using the Sony  $\alpha 7S2$  camera. The dataset comprises 1,865 images for training, 234 validation images, and 598 testing images, all with a resolution of  $4240 \times 2832$  pixels. The noisy images are taken with short exposure times, whereas the corresponding clean images are captured with longer exposure times and are thus assumed to be noiseless. The exposure-time ratios between the long and short-exposure images are set at 100, 250, and 300.

Additionally, we test our denoising network on the ELD Sony dataset [52]; it consists of 60 low-light noisy raw images also captured using the same Sony  $\alpha 7S2$  camera model as the SID dataset.

### C.3. Training Configurations

Here we give more training details of our diffusion model and denoising network. Note that our method operates in the RAW image domain, therefore, the Bayer arrays are packed into four channels [11] (the spatial resolution is reduced by a factor of two in each dimension correspondingly) before being fed into diffusion or denoising networks. This step is not shown in Fig. 2 of the main paper for clarity.

**Diffusion Model Training.** Before training the diffusion model, we perform data resampling: for camera settings with fewer than 100 training pairs, we augment the data by repeating samples until the count reaches 100. We train our diffusion model using the Adam optimizer for 1,000 epochs. The learning rate is initially set to  $1e-4$  and decays to  $1e-5$  by the end of the training, using a cosine annealing schedule. The batch size is set to 12. We randomly crop  $512 \times 512$  patches from the training samples. All Sony training pairs from the SID dataset are used for training, with their ISO values and exposure time ratios encoded.

After the training is complete, we use clean images in the SID training set to generate synthetic noisy images as described above.

**Denosing Network Training.** To assess the quality of the synthetic data, we train denosing networks using the  $L1$  loss between the network’s output and the reference clean image, then evaluate their denosing performance. For a fair comparison, we use the same U-Net architecture employed in [11]. The denosing networks are trained using the Adam optimizer for 500 epochs. During training, the batch size is 4, and we randomly crop  $256 \times 256$  patches, applying random horizontal flips for data augmentation.

#### C.4. Clean-Noisy Pair Generation

During diffusion model inference, we use clean images from the SID training set to generate synthetic data. As our diffusion network operates at an image size of  $512 \times 512$ , each clean image is first divided into overlapping patches of  $512 \times 512$  pixels, with a  $1/4$  patch size overlap. A pixel coordinate map is also computed for each patch. We condition our network on these cropped patches, the corresponding pixel coordinate maps, and the camera settings to generate noise patches. Each noise patch is then added to its conditioned clean patch to create a noisy patch. These clean and noisy patches are paired together to form clean-noisy pairs subsequently used for training the denosing network.

#### D. Evaluation Protocol: Noise Mean and Variance

In this section, we provide the detailed procedure for computing the noise mean and variance used for evaluating noise quality, as mentioned in Sec. 4.1 of the main paper.

The specific analysis procedure is indicated in Fig. S1. Assuming the value range of the clean images falls within the interval  $[0, M]$  (e.g., for an 8-bit image,  $M = 255$ ), we iterate over each clean pixel value. Given a clean pixel value  $i$ , all pixels in the clean images with this value are identified and their positions recorded. Subsequently, the pixels in the corresponding noise images at the same positions are retrieved. This process yields multiple noise values for

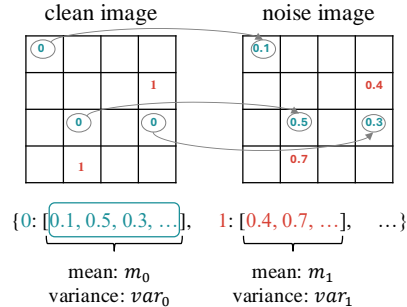


Figure S1. Noise mean and variance calculation. For a specific clean value  $i$ , we gather corresponding noise values from the noise image and compute their mean and variance. Here, we illustrate the clean values 0 and 1, for example. We perform the same procedure for all the clean values (e.g., for an 8-bit image, the clean values range from 0-255).

clean pixel value  $i$ , from which the noise mean value  $m_i$  and variance  $var_i$  are computed. Some examples are illustrated in Fig. 5 of the main paper, where we compare these two statistics between real noise images and synthetic noise images. Correctly approaching these values is crucial for precisely training our denosing network.

#### E. More Discussions

##### E.1. Influence of Training-Data Diversity

In the main paper, we presented an ablation study investigating the influence of training data diversity. We trained a separate denosing network using less synthetic data than in our standard configuration. Here, we provide details about both our standard and limited-data configurations.

**Standard Configuration.** The original SID training set contains varying numbers of scenes across different camera settings, with some settings having very few scenes. For instance, the camera setting with ISO 6400 and ratio 300 has only one unique scenes. With our data generation model, however, we can leverage all the clean images in the SID training set to generate numerous training pairs for each camera setting. Specifically, if there are  $K$  clean images in total, we can generate  $K$  noisy images for each camera setting by conditioning our diffusion model on the camera setting embedding. Furthermore, since DDPM sampling is non-deterministic, different random seeds allow us to generate infinite noisy images from a single clean image. For efficiency, though, we generate a certain number of noisy images for each camera setting. For any setting with fewer than 6 unique clean images ( $K_i < 6$ ), we randomly sample  $30 - K_i$  additional clean images from other settings to augment the clean image number, then generate noisy images from both the original and augmented clean images.

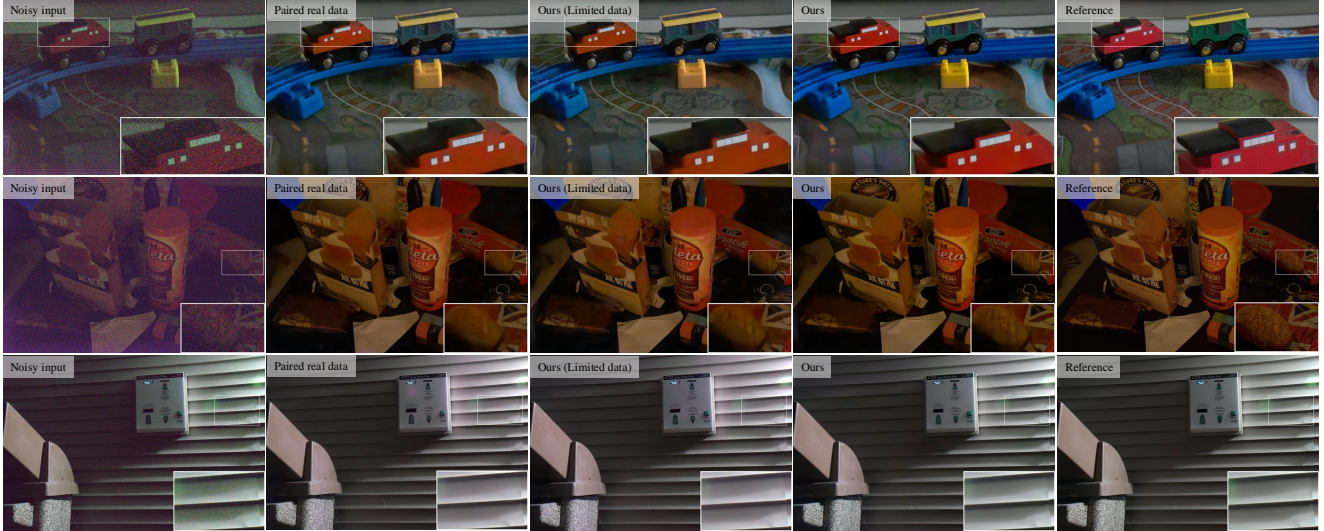


Figure S2. Ablation study on influence of training-data diversity for denoising. **Paired real data:** The denoising network is trained using real data from the SID Sony training set [11], where some camera settings have very few unique scenes (e.g., the camera setting with ISO 6400 and ratio 300 has only one unique scenes). **Ours:** The denoising network is trained with our full set of synthetic data, where camera settings with limited unique scenes are augmented by scenes from other settings. Synthetic data is generated using the augmented scenes. **Ours (Limited data):** The denoising network is trained with limited synthetic data, where the number of scenes for each camera setting matches the original SID training set. The above three test samples from the SID testing set: (1) ISO 6400, ratio 300 (only one unique clean image in the original SID training set); (2) ISO 12800, ratio 100 (three unique clean images originally); and (3) ISO 800, ratio 100 (two unique clean images originally). It can be observed that the denoising performance improves with more synthetic data.

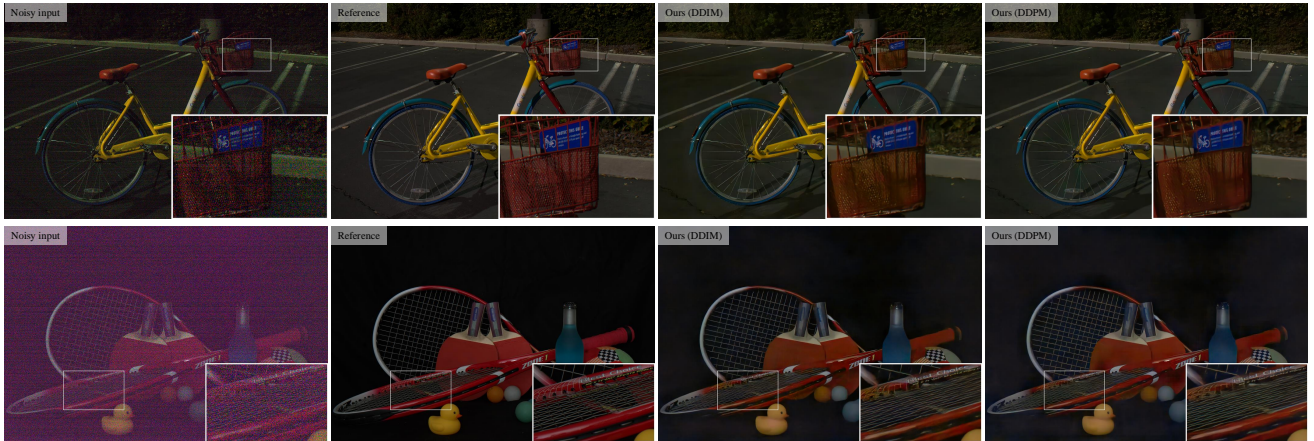


Figure S3. Comparison of denoising results from networks trained by synthetic data generated by DDIM [45] and DDPM [25] sampling methods. We use 100 steps for DDIM sampling, and 1000 steps for DDPM sampling. It shows that DDIM can also generate visually satisfactory results, and can serve as an efficient alternative to our method.

For settings with more than 6 clean images, we use only the original clean images for data generation.

**Limited-Data Configuration.** Here, we generate data without clean image augmentation. Specifically, for each camera setting with  $K_i$  clean images in the SID training set, we generate noisy images using only these  $K_i$  clean images. Therefore, the denoising network under this limited-data

configuration uses the same number of scenes per camera setting as in the original SID training set.

As a result, these two settings consist of different number of synthetic pairs (only synthetic pairs, no real pairs included) for training the denoising networks.

Fig. S2 presents a visual comparison using three test samples from the SID testing set: (1) ISO 6400, ratio 300 (only one unique clean image in the original SID training

set); (2) ISO 12800, ratio 100 (three unique clean images originally); and (3) ISO 800, ratio 100 (two unique clean images originally). As shown, *Ours* produces better results than *Ours (Limited data)*, benefiting from the additional synthetic training data. This further demonstrates that denoising performance improves with more synthetic data.

## E.2. Sampling Method

As mentioned in the main paper, we use DDIM sampling as an efficient alternative for generating data. Table 3 of the main paper shows that DDIM achieves satisfactory performance with a minor drop compared to DDPM-generated data. Qualitative results in Fig. S3 further demonstrate that DDIM provides nearly comparable visual quality to DDPM, offering a practical alternative for faster generation. To better understand the performance difference, we analyze noise statistics by computing the mean and variance. In Fig. S5, we provide comparisons of the noise statistics between DDPM and DDIM. As can be observed, DDIM sampling tends to yield low-light noise with lower variance.

## E.3. Noise Decomposition

**Implicit Noise Decomposition.** While noise decomposition on real noise images is not possible due to the absence of ground-truth for the signal-dependent and signal-independent components, the conditional generation capability of our diffusion model allows us to perform implicit noise decomposition on the generated noise.

In Fig. S4 (a), (b), and (d)-(f), we visualize the clean image, the ground-truth noise, the noise generated by our full model, and the decomposed components. To achieve this decomposition, we condition the diffusion model on a fully black clean image (a zero map), changing the generation process from  $\tilde{\mathbf{n}}_t = f_\theta(\tilde{\mathbf{n}}_{t-1}, t, \mathbf{x}, \mathbf{c}, \mathbf{z})$  (as described in Sec. 3.1 of the main paper) to  $\tilde{\mathbf{n}}_t = f_\theta(\tilde{\mathbf{n}}_{t-1}, t, \mathbf{0}, \mathbf{c}, \mathbf{z})$ . This modification removes the signal information, resulting in the generation of only the signal-independent noise component, shown in Fig. S4 (e). Subtracting the signal-independent noise from the full noise isolates the signal-dependent noise component, as shown in Fig. S4 (f). Notably, the row noise and low-frequency noise are captured in Fig. S4 (e), whereas Fig. S4 (f) contains primarily a shot-noise-like pattern.

We further analyze the statistics of different noise components. In Fig. S4 (g) and (j), we compare the variance and mean values of our generated noise with those of the real noise; they are calculated using the method described in Sec. D. The results indicate that our method produces a noise distribution similar to the real noise. In Fig. S4 (h) and (k), we present the statistics of the signal-independent noise; they clearly show that the noise mean and variance are independent of the clean pixel values. Conversely, Fig. S4 (i) and (l) depict the statistics of the signal-dependent noise, demonstrating that both the noise variance and mean are

correlated with the clean pixel values.

This noise decomposition capability allows our diffusion model to generate either full noise maps or only signal-independent noise maps (dark frames). Dark frames are valuable for computing dark shadings, as discussed in Sec. 2 of the main paper, which can further aid in the denoising process.

Drawing inspiration from [18], this noise decomposition could be further used for faster full noise generation by using our diffusion model to generate dark frames and a fitted Poisson distribution for signal-dependent noise. Generating only a few dark frames with the diffusion model would allow for on-the-fly noise generation, which is impossible due to the lengthy diffusion process.

**Additional Evidence Supporting the Effectiveness of the Two-Branch Network.** Meanwhile, we also apply the same decomposition process to the noise generated by the UNet-only architecture, with the results shown in Fig. S4 (m)-(u). It is evident that the signal-independent and signal-dependent components are not fully disentangled. For instance, in Fig. S4 (o), low-frequency noise is still present at the bottom of the signal-dependent component. Moreover, we can clearly see This performance difference between the two architectures further highlights the effectiveness of the two-branch architecture in modeling signal-independent and signal-dependent noise, simplifying the network’s learning process.

## E.4. Noise Histogram

Here, we present the histogram of generated noise from different ablation variants. As shown in Fig. S6, our full model with DDPM sampling generates noise that aligns more closely with the distribution of real noise.

## F. More Visual Comparisons

In this section, we provide more visual comparisons of denoising results from different networks trained on data synthesized using different methods. Fig. S7 - Fig. S11 are examples from the SID test set and Fig. S12 - Fig. S13 are examples from the ELD test set. Our method demonstrates effectiveness in handling row noise, as evidenced in the second and third examples of Fig. S7 and the first example of Fig. S8. Additionally, it excels at mitigating low-frequency noise, particularly visible in the second and third examples of Fig. S9. Moreover, our approach enhances detail retention in denoising results, for example, producing clearer text compared to other methods, as shown in the second and third examples of Fig. S9 and throughout Fig. S12.

## G. Ethics Considerations

This paper addresses the task of noise synthesis for image denoising, primarily aimed at enhancing image quality in low-light photography. While the technique can improve

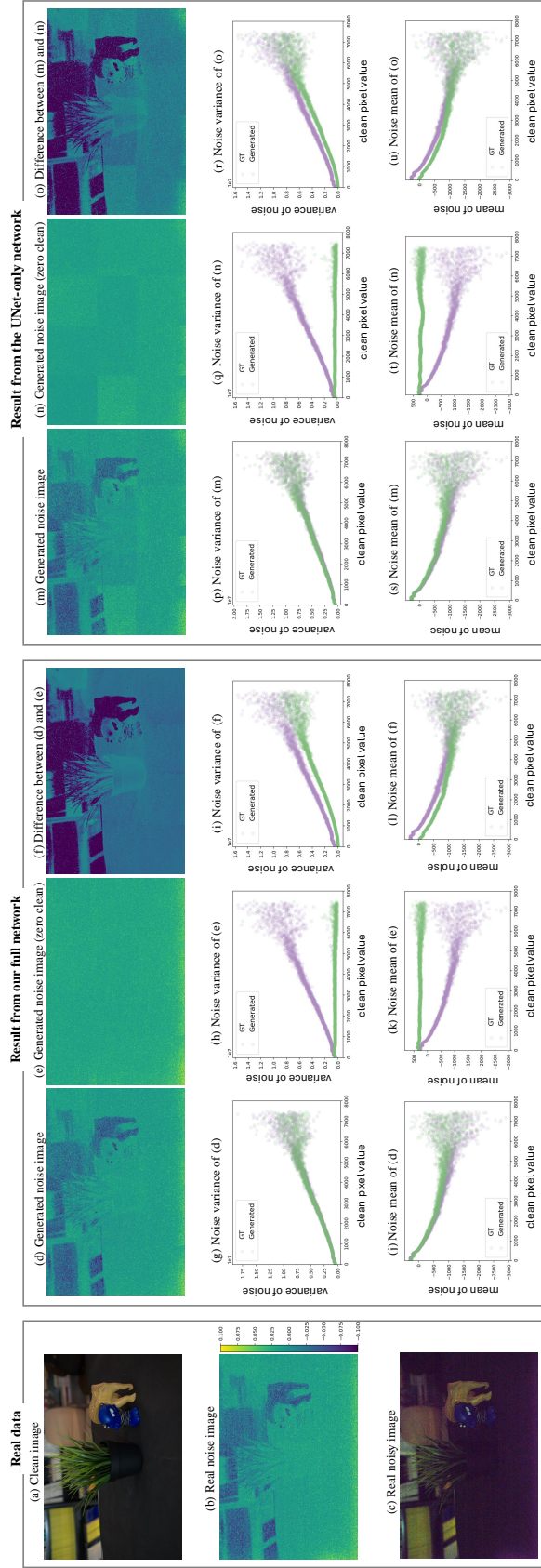


Figure S4. Noise decomposition of the generated noise. (a) A clean image from the SID Sony test set with ISO 4000 and ratio 300. (b), (c) The corresponding real noise image and noisy image. (d) The noise image generated by our full model. (e) When the clean image input,  $\mathbf{x}$ , is set to a full zero map, the noise generated is the signal-independent noise component. (f) The signal-dependent noise component, obtained by subtracting (e) from (d). (g), (j) The noise variance and mean of (d). (h), (k) The noise variance and mean of (e). (i), (l) The noise variance and mean of (f). (m)-(u) The results from the UNet-only network. For the visualized noise images, different noise values are represented by varying colors, with the color bar displayed on the right of (b). The statistics of the generated noise are shown in green, and the statistics of the real noise are shown in purple. The results indicate that our full model generates noise distributions closely resembling real noise. The mean and variance of the isolated signal-independent noise are independent of the clean pixel values. Conversely, the mean and variance of the signal-dependent noise are both correlated with the clean pixel values. While for the UNet-only network, it can be observed that the signal-independent and signal-dependent components are not fully disentangled, as shown in (m)-(o).

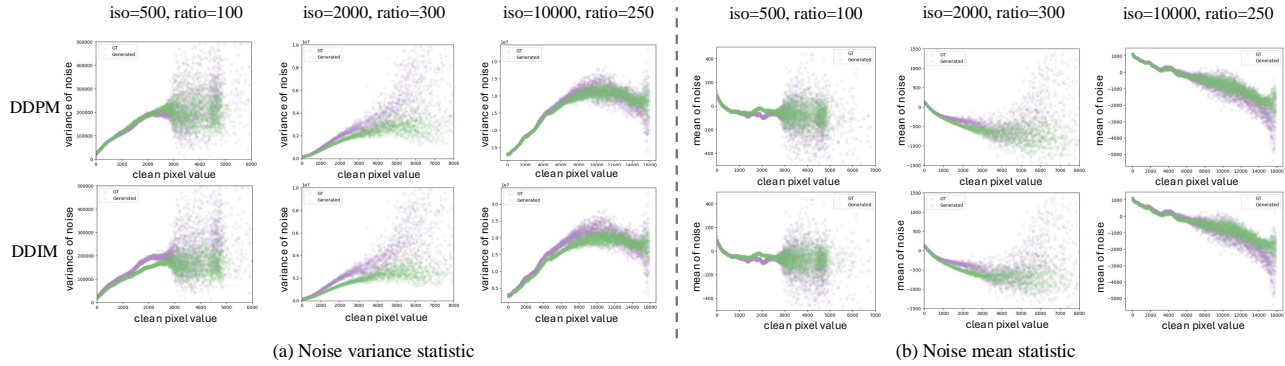


Figure S5. Comparison of noise statistics between DDIM, DDPM, and real noises across three different camera settings. The primary performance difference between the two sampling methods lies in the variance of the **generated noises**, with DDIM sampling exhibiting a larger variance gap from the **real noise** compared to DDPM sampling.

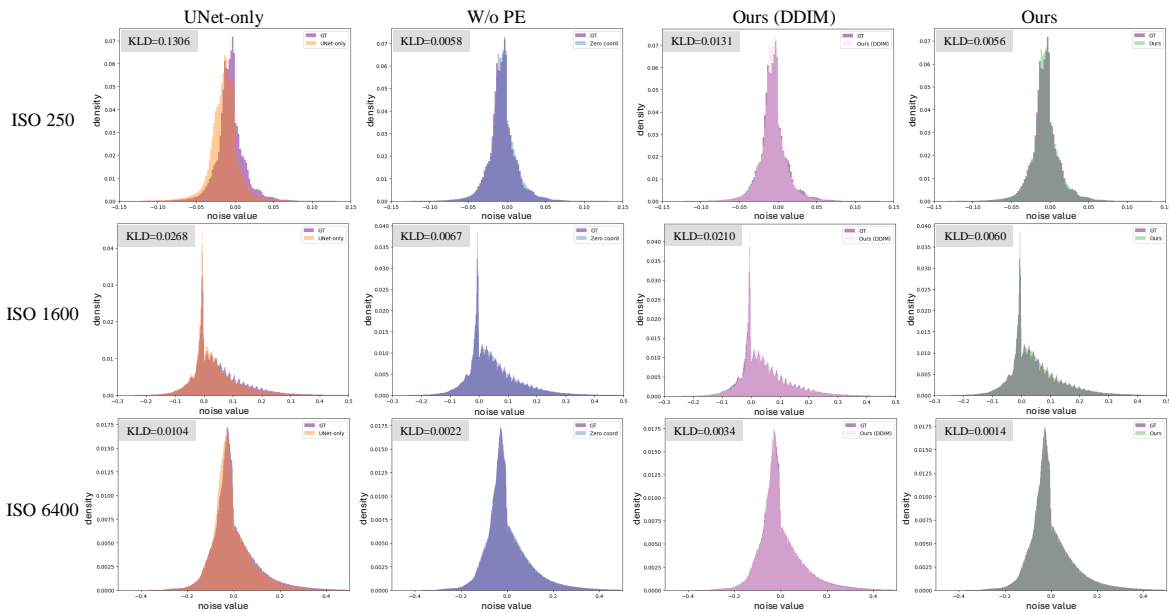


Figure S6. Histogram of noise values and Kullback-Leibler (KL) divergence between generated noise and **real noise** for four ablation variants: the **UNet-only** architecture, model without positional encoding (**W/o PE**), our full model with DDIM sampling (**Ours (DDIM)**) and our full model with DDPM sampling (**Ours**). Evaluations are conducted across three different ISO settings. The results produce by our full model are closest to the real noise distribution.

photographic quality for general use, it also has implications for fields such as surveillance and medical imaging, where denoising and noise synthesis could potentially impact data integrity if misused. We recognize the importance of transparency in synthetic data applications and encourage responsible use to avoid unintended consequences, such as creating misleadingly “cleaned” images in sensitive areas where accurate data representation is essential.

No known negative societal impacts are associated with this research, and we encourage users to apply these methods ethically.

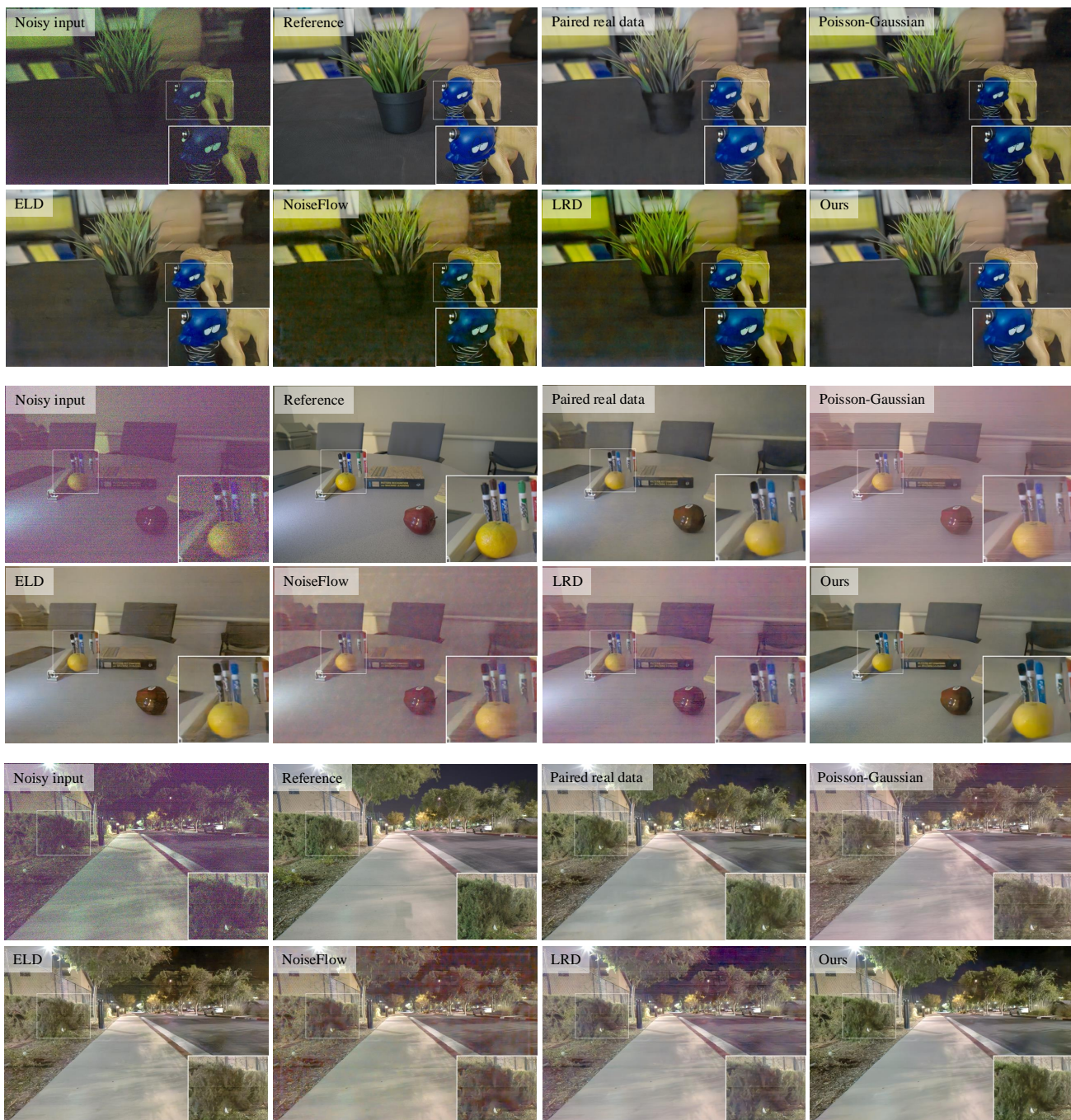


Figure S7. Visual comparisons of denoising results from networks trained on data synthesized using different methods, alongside comparisons with a model trained on real clean-noisy pairs from the SID training set. All test samples are from the SID Sony test set. Results here are processed by the same gamma correction ( $\mathbf{I}_{out} = \mathbf{I}_{in}^{1/1.6}$ ) for a clearer view as the main paper.

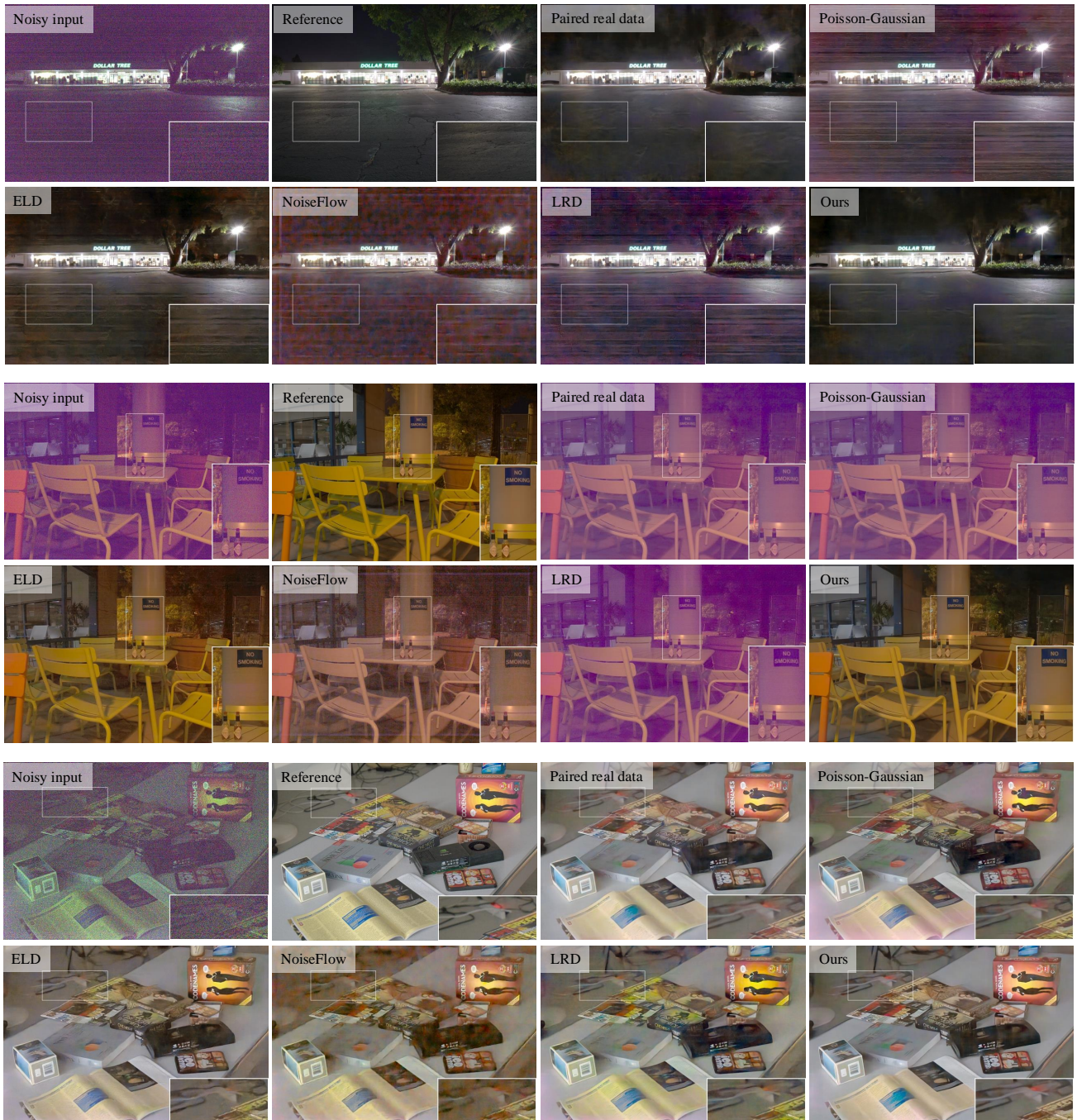


Figure S8. Visual comparisons of denoising results from networks trained on data synthesized using different methods, alongside comparisons with a model trained on real clean-noisy pairs from the SID training set. All test samples are from the SID Sony test set. Results here are processed by the same gamma correction ( $\mathbf{I}_{out} = \mathbf{I}_{in}^{1/1.6}$ ) for a clearer view as the main paper.

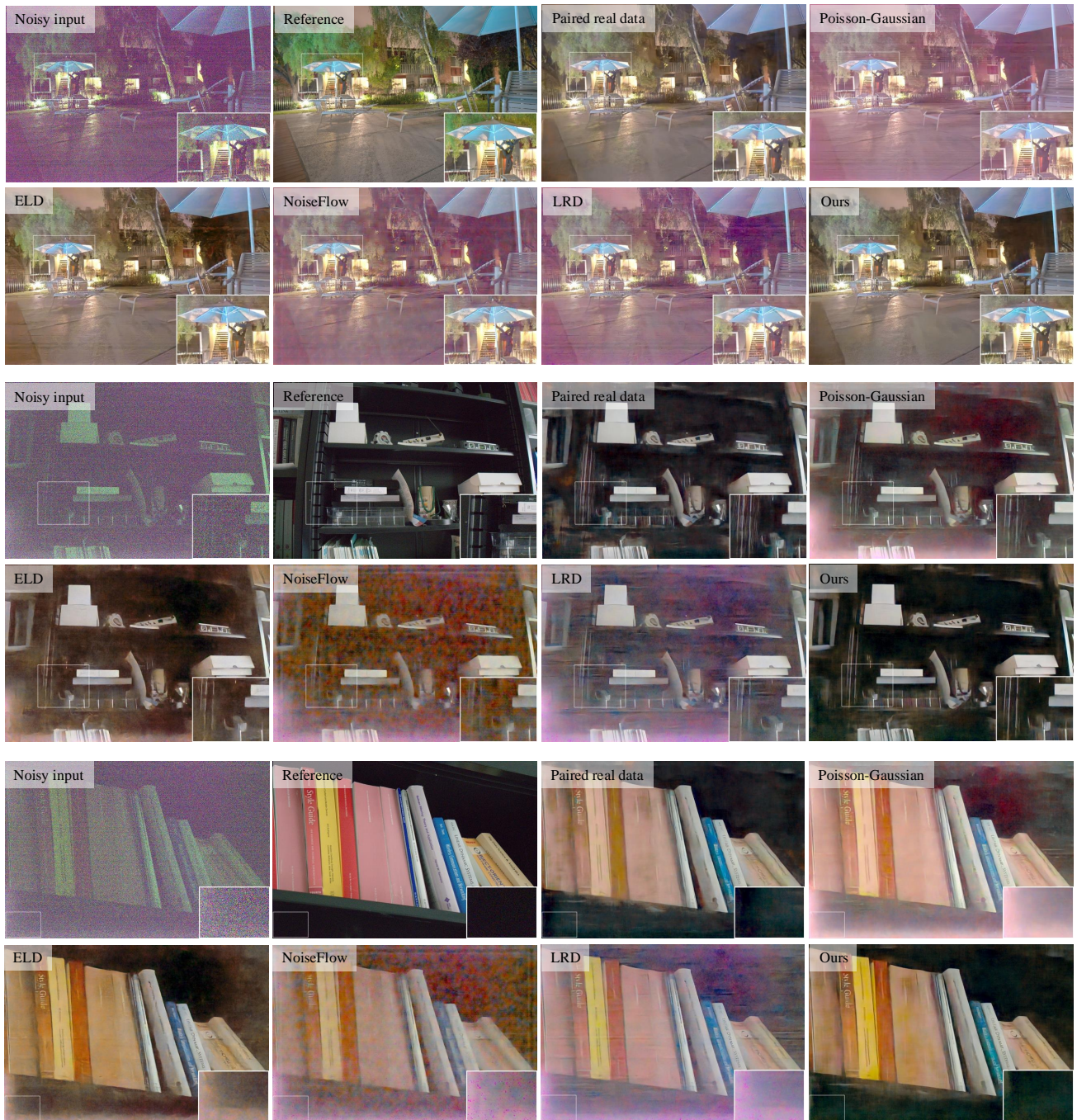


Figure S9. Visual comparisons of denoising results from networks trained on data synthesized using different methods, alongside comparisons with a model trained on real clean-noisy pairs from the SID training set. All test samples are from the SID Sony test set. Results here are processed by the same gamma correction ( $\mathbf{I}_{out} = \mathbf{I}_{in}^{1/1.6}$ ) for a clearer view as the main paper.

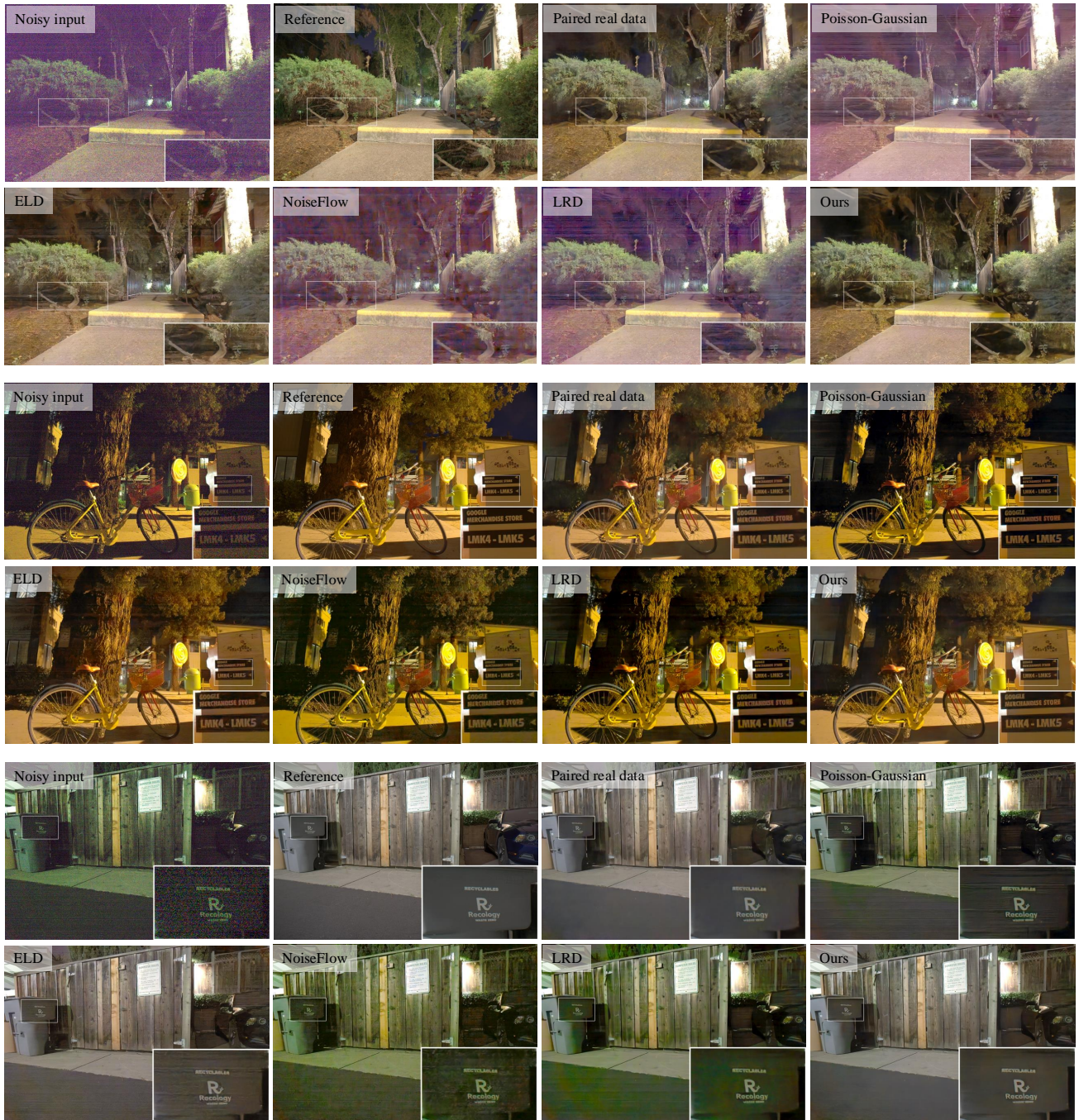


Figure S10. Visual comparisons of denoising results from networks trained on data synthesized using different methods, alongside comparisons with a model trained on real clean-noisy pairs from the SID training set. All test samples are from the SID Sony test set. Results here are processed by the same gamma correction ( $I_{out} = I_{in}^{1/1.6}$ ) for a clearer view as the main paper.

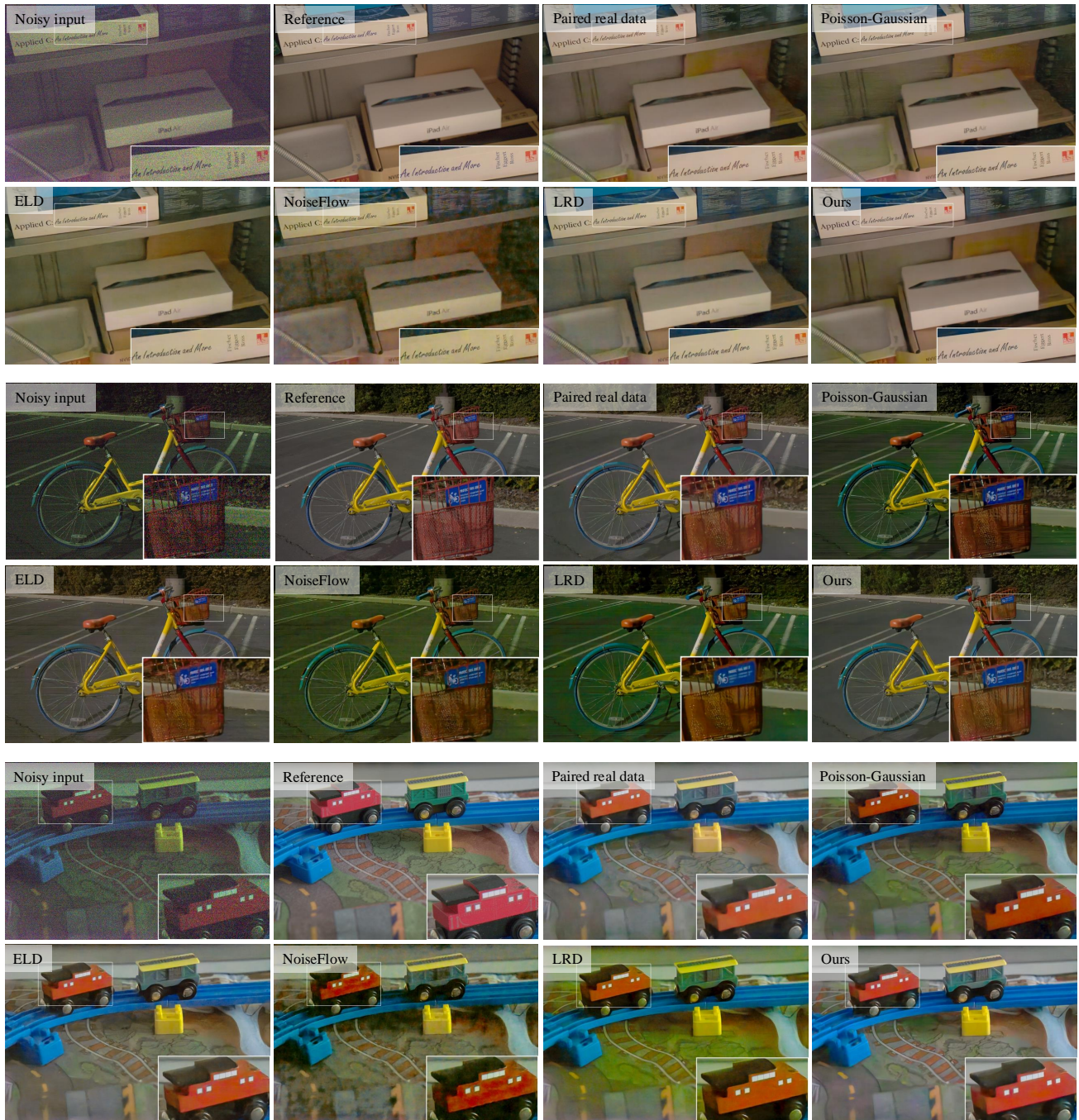


Figure S11. Visual comparisons of denoising results from networks trained on data synthesized using different methods, alongside comparisons with a model trained on real clean-noisy pairs from the SID training set. All test samples are from the SID Sony test set. Results here are processed by the same gamma correction ( $\mathbf{I}_{out} = \mathbf{I}_{in}^{1/1.6}$ ) for a clearer view as the main paper.

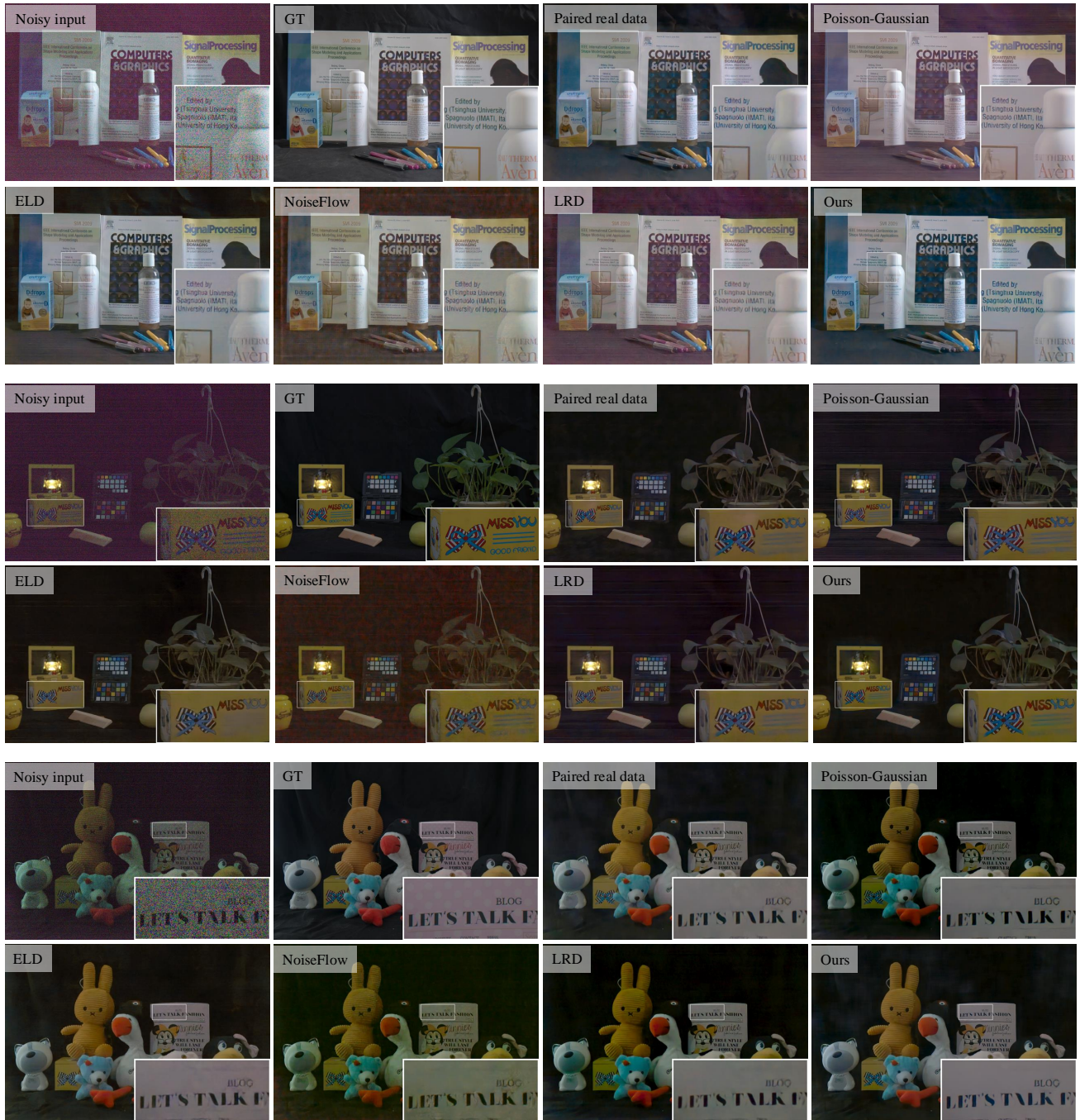


Figure S12. Visual comparisons of denoising results from networks trained on data synthesized using different methods, alongside comparisons with a model trained on real clean-noisy pairs from the SID training set. All test samples are from the ELD test set. Results here are processed by the same gamma correction ( $I_{out} = I_{in}^{1/1.6}$ ) for a clearer view as the main paper.

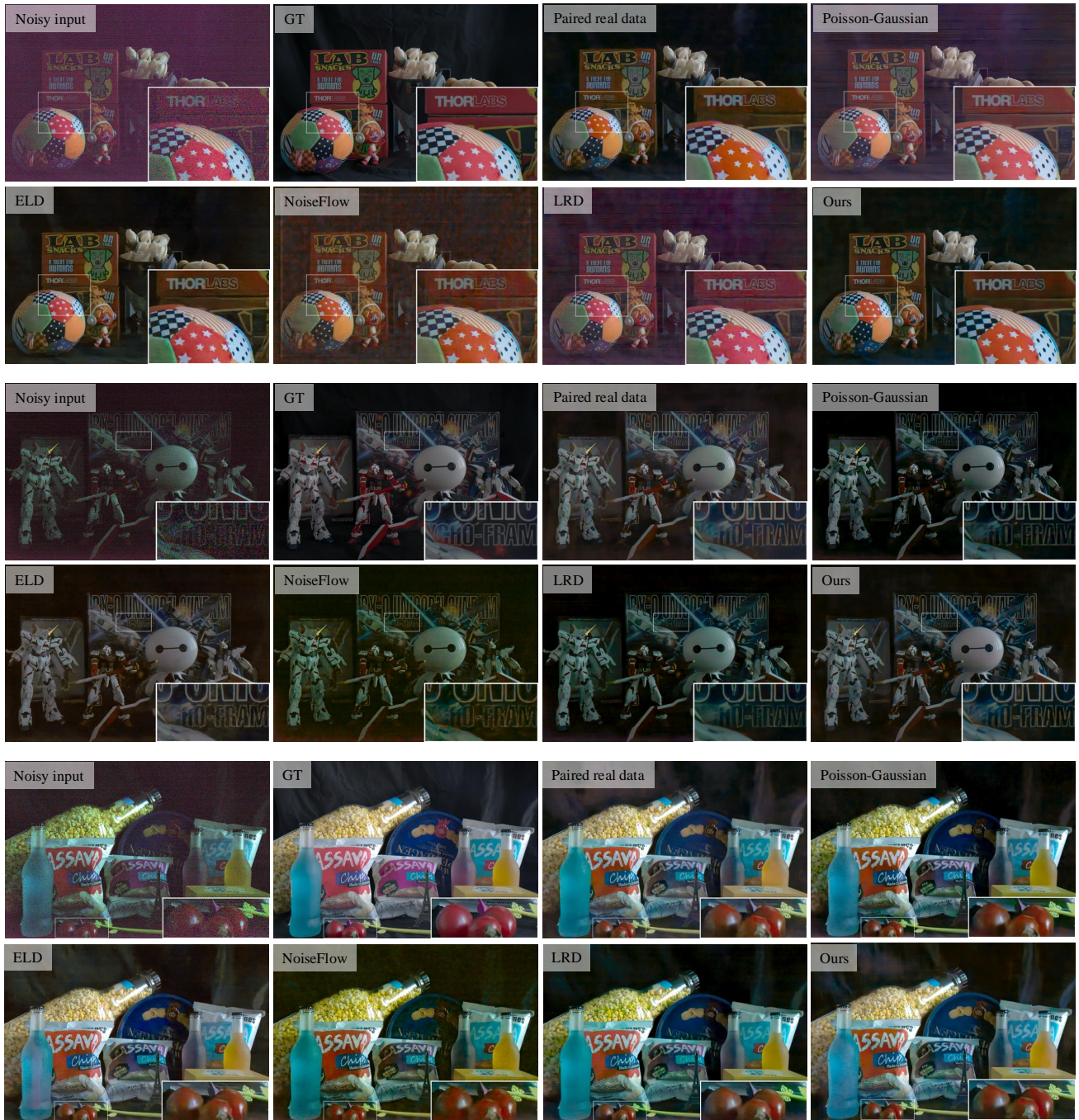


Figure S13. Visual comparisons of denoising results from networks trained on data synthesized using different methods, alongside comparisons with a model trained on real clean-noisy pairs from the SID training set. All test samples are from the ELD test set. Results here are processed by the same gamma correction ( $I_{out} = I_{in}^{1/1.6}$ ) for a clearer view as the main paper.